provide strong evidence that biologically relevant tribological properties are preserved in the fossil teeth.

Nanoindentation revealed mean hardness values from ~1 GPa for secondary dentine to ~6 GPa for enamel (Fig. 3C). Hardness and wear rates are related as expected for AMNH 5896 (Fig. 3D), and hardnesses were similar among *Edmontosaurus* individuals (Fig. 3C). Hardness-based wear models for all three dinosaurs also wore to a morphology matching naturally worn batteries, including crests where enamel is absent and branched ridges (fig. S7).

In a phylogenetic context, these histological, biomechanical, and simulation data demonstrate how hadrosaurids evolved mammal-like grinding capacity. The primitive condition, in Hadrosauridae, seen in *Edmontosaurus* and most taxa (fig. S3), was a dual-function slicing-grinding system, presumably for the consumption of fibrous, moderately tough plants (*2*). The leading teeth have an inclined slicing plane, whereas all others form a file-like pavement. Highly wear-resistant enamel forms crests in all upper battery teeth but only in the lead teeth in the lower battery, because enamel was worn away before the teeth migrated across the chewing surface (Figs. 2A and 4A). Wear-resistant mantle dentine is the tissue that takes over the crest-forming role in the lower batteries (Fig. 4A and fig. S5). The inclined slicing faces in the leading teeth are composed of giant tubule curtains with intermediate wear resistance, spanning between the wear-resistant mantle dentine crests and the high-wear orthodentine basins (Fig. 2D and fig. S5). Large individual and branched giant tubules formed intermediate-height ridges partitioning the basins (Fig. 4A and fig. S5). Modeling shows that they influenced basin depth at each tooth position [greater sliding distance = greater scour (*23*)] and probably provided for finer grinding of plants than did major crests (fig. S5). Coronal cementum is prevalent, as in mammalian grinding teeth (Figs. 2D and 4A). It similarly served as a bridge minimizing stress singularities on the hard brittle crests, but also bound teeth together (fig. S5). Abscess-preventing secondary dentine is present only where the pulp cavity was locally breached and, unlike in mammalian grinding teeth, didn't substantially contribute to basin formation through wear.

The distribution of these characters phylogenetically shows that longitudinal giant tubules and secondary dentine evolved at the base of Ornithopoda, probably for abscess prevention in association with dental occlusion (fig. S3). Transverse giant tubules subsequently appeared in hadrosauroideans for steeper-angled slicing. The remaining tissues (mantle dentine and extensive coronal cementum) are primitive for Hadrosaurids and evolved as innovations for combined slicing and grinding (fig. S3). Tissue-complex modifications appear to have allowed for diversification into specialized ecological niches (fig. S3). Some taxa evolved teeth with coarse grinding pavements across the entire chewing area, presumably for processing tough plant matter (figs. S2 and S3). This was achieved through the loss of transversely oriented giant tubules, so slicing plane formation and basin partitioning couldn't occur. In other taxa, grinding capacity was completely lost and the teeth were specialized for high-angle slicing (fig. S3). In these batteries, transversely oriented giant tubules radiate throughout the teeth, so shearing faces formed at all wear stages across the chewing surfaces.

Hadrosaurids evolved the most histologically and biomechanically sophisticated dentitions known among reptiles, and these rivaled those of advanced herbivorous mammals in complexity. Three-dimensional tribological modeling allows for an improved understanding of tissue-level contributions to dental form and function. The ability to measure wear-relevant properties in fossils provides a new approach to study biomechanics throughout evolution. Such inferences will be enlightening across major mammalian and reptilian diversifications involving dental and dietary changes (*24, 25*).

References and Notes

1. V. S. Williams, P. M. Barrett, M. A. Purnell, *Proc. Natl. Acad. Sci. U.S.A.* **106**, 11194 (2009).
2. J. S. Tweet, K. Chin, D. R. Braman, N. L. Murphy, *Palaios* **23**, 624 (2008).
3. R. S. Lull, N. E. Wright, *Spec. Pap. Geol. Soc. Am.* **40**, 1 (1942).
4. J. H. Ostrom, *Bull. Am. Mus. Nat. Hist.* **122**, 1 (1961).
5. D. B. Norman, D. B. Weishampel, in *Biomechanics in Evolution*, J. M. V. Rayner, R. J. Wootton, Eds. (Cambridge Univ. Press, Cambridge, 1991), pp. 161–181.
6. D. B. Weishampel, *Acta Palaeontol. Pol.* **28**, 271 (1983).
7. G. M. Erickson, *Proc. Natl. Acad. Sci. U.S.A.* **93**, 14623 (1996).
8. A. Prieto-Márquez, *Zool. J. Linn. Soc.* **159**, 435 (2010).
9. D. C. Evans, C. A. Forster, R. R. Reisz, in *Dinosaur Provincial Park: A Spectacular Ancient Ecosystem Revealed*, P. Currie, E. Koppelhus, Eds. (Indiana Univ. Press, Bloomington, IN, 2005), pp. 349–366.
10. B. Peyer, *Comparative Odontology* (Univ. of Chicago Press, Chicago, 1968).
11. S. Hillson, *Teeth* (Cambridge Univ. Press, Cambridge, 1986).
12. C. M. Janis, M. Fortelius, *Biol. Rev. Camb. Philos. Soc.* **63**, 197 (1988).
13. P. L. Lucas, *Dental Functional Morphology: How Teeth Work* (Cambridge Univ. Press, Cambridge, 2004).
14. W. J. Schmidt, A. Keil, *Polarizing Microscopy of Dental Tissues* (Pergamon Press, Oxford, 1971).
15. J. Leidy, *Smith. Contrib. Knowl.* **14**, 1 (1865).
16. R. J. Butler *et al*., *Proc. Biol. Sci.* **277**, 375 (2010).
17. Materials and methods are available as supporting materials on *Science* Online.
18. J. F. Archard, *J. Appl. Phys.* **24**, 981 (1953).
19. M. M. Khruschov, *Wear* **28**, 69 (1974).
20. J. D. Currey, R. M. Abeysekera, *Arch. Oral Biol.* **48**, 439 (2003).
21. W. M. Johnson, A. J. Rapoff, *J. Mater. Sci. Mater. Med.* **18**, 591 (2007).
22. W. G. Sawyer, *Tribol. Lett.* **17**, 139 (2004).
23. J. F. Archard, W. Hirst, *Proc. R. Soc. London Ser. A* **236**, 397 (1956).
24. K. Schwenk, Ed., *Feeding: Form, Function and Evolution in Tetrapod Vertebrates* (Academic Press, San Diego, CA, 2000).
25. R. R. Reisz, H. D. Sues, in *Evolution of Herbivory in Terrestrial Vertebrates: Perspectives from the Fossil Record,* H. D. Sues, Ed. (Cambridge Univ. Press, Cambridge, 2000), pp. 9–41.

Acknowledgments: We thank W. Nix, A. Prieto-Marquez, P. Lee, P. Druckenmiller, C. Taylor, and E. McCumiskey for their assistance and NSF (grant EAR 0959029 to G.M.E. and M.A.N.) for research funding. Data described in the paper are archived by the Computer Support Group of the Department of Biological Science at Florida State University as databases S1 to S19.

Supplementary Materials

www.sciencemag.org/cgi/content/full/338/6103/98/DC1
Materials and Methods
Supplementary Text
Figs. S1 to S7
Table S1
References (*26–40*)
Captions for Databases S1 to S19

9 May 2012; accepted 24 August 2012
10.1126/science.1224495

Rapid Acceleration Leads to Rapid Weakening in Earthquake-Like Laboratory Experiments

J. C. Chang,[1] D. A. Lockner,[2] Z. Reches[1]*

After nucleation, a large earthquake propagates as an expanding rupture front along a fault. This front activates countless fault patches that slip by consuming energy stored in Earth's crust. We simulated the slip of a fault patch by rapidly loading an experimental fault with energy stored in a spinning flywheel. The spontaneous evolution of strength, acceleration, and velocity indicates that our experiments are proxies of fault-patch behavior during earthquakes of moment magnitude (M_w) = 4 to 8. We show that seismically determined earthquake parameters (e.g., displacement, velocity, magnitude, or fracture energy) can be used to estimate the intensity of the energy release during an earthquake. Our experiments further indicate that high acceleration imposed by the earthquake's rupture front quickens dynamic weakening by intense wear of the fault zone.

Large earthquakes initiate at a small nucleation area and grow as propagating rupture fronts (*1*, *2*) (Fig. 1A). The propagating front activates a multitude of fault patches that undergo intense deformation (Fig. 1, B and C). Before the front arrives, the stress μ on each patch is generally lower than its static strength μ_s [both stress and strength are presented as the friction

coefficient, μ = (shear stress/normal stress)]. If the arriving front raises the stress to the static strength level, the patch strength may drop (*1*) (Fig. 1B), and it slips while releasing elastic energy stored in the rocks, and eventually it decelerates and stops. This model is widely accepted (*1*–*7*), yet the evolution of strength, velocity, and energy partitioning are poorly constrained (*2*, *4*).

In stick-slip experiments (*3*, *7*), the above earthquake sequence was simulated by loading an experimental fault until it spontaneously generated an earthquake-like event (Fig. 1B). However, these experiments are limited to tiny displacements (*3*, *6*, *7*) that are five to six orders of magnitude less than large earthquake displacements. To circumvent this limitation, earthquake modelers relied on constitutive equations, like rate- and state-friction, based on steady-state friction data.

We simulated fault-patch slip during large earthquakes by employing one central concept: abruptly

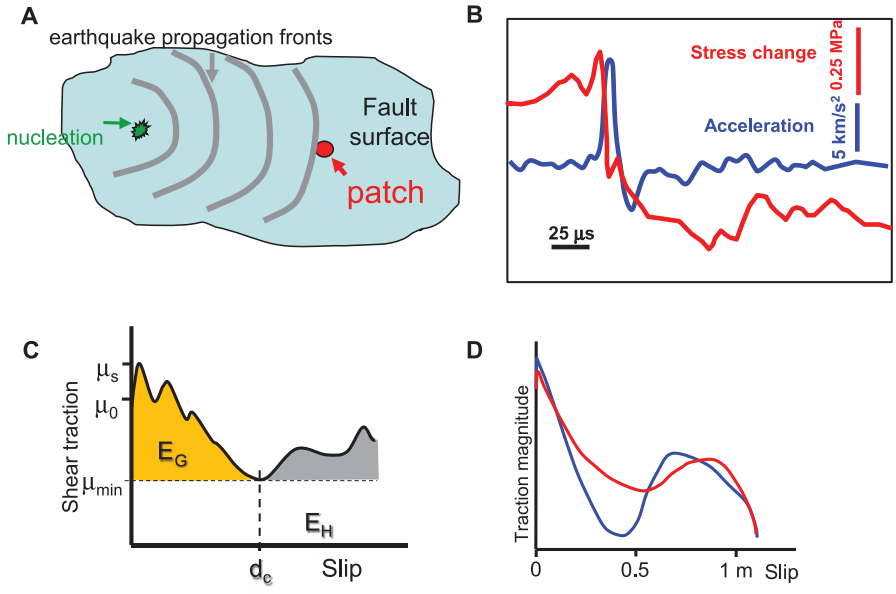

Fig. 1. Stress and energy on a fault patch during an earthquake. (**A**) A fault patch activated by a propagating earthquake rupture. (**B**) Shear stress and slip acceleration during a stick-slip event along an experimental granite fault (*3*). (**C**) Conceptual evolution of shear traction on a fault patch during an earthquake (*2*). E_H, frictional heat energy; E_G, breakdown energy. (**D**) Calculated traction evolution of two fault patches of Northridge earthquake (*2*).

[1]Geology and Geophysics, University of Oklahoma, 100 East Boyd Street, Norman, OK 73019, USA. [2]U.S. Geological Survey, 345 Middlefield Road, Menlo Park, CA 94022, USA.

*To whom correspondence should be addressed. E-mail: reches@ou.edu

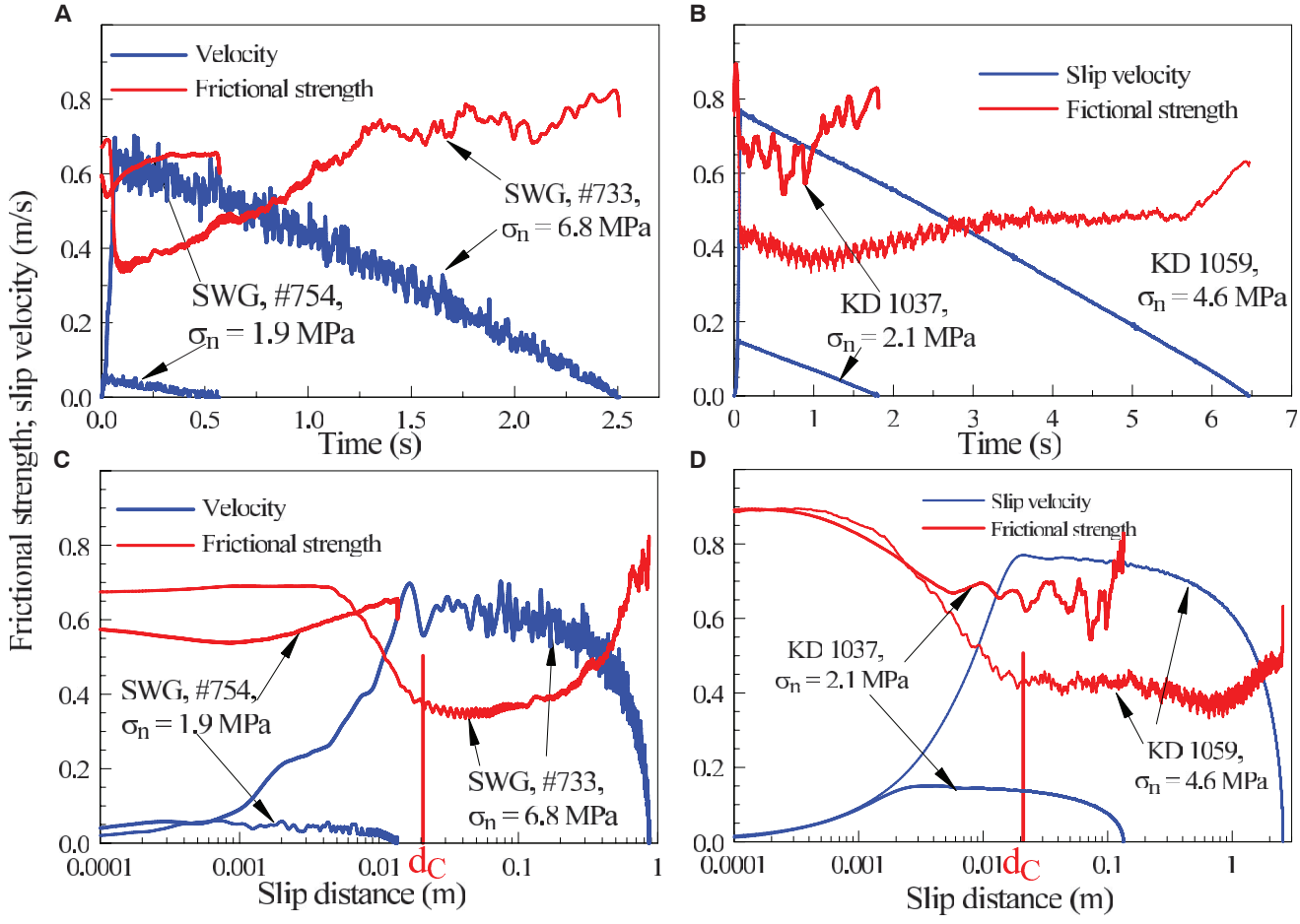

Fig. 2. The evolution of frictional strength and slip velocity in ELSE experiments with respect to (**A** and **B**) time and (**C** and **D**) slip distance (*9*). (A and C) Two runs with SWG loaded with E_C = 0.007 m (#754) and E_C = 0.43 m (#733). (B and D) Two runs with KD loaded with E_C = 0.09 m (#1037) and E_C = 1.20 m (#1059).

deliver a finite amount of energy to an experimental fault patch that spontaneously dissipates the energy without operator intervention. We used a rotary-shear apparatus, in which a ring-shaped fault slips at velocities of up to 1 m/s, at normal stresses of up to 30 MPa (*8*, *9*). We conducted 42 experiments on Sierra White granite (SWG) samples and 24 experiments on Kasota dolomite (KD) samples. Each experiment starts by spinning a 225-kg disk-shaped flywheel to a prescribed angular velocity; during this stage, the sample remains stationary (*9*). Then, a fast-acting clutch engages the sample-half, forcing it to rotate with the flywheel until all stored kinetic energy is dissipated. We refer to this experiment as an "earthquake-like slip event" (ELSE) (table S1). The total energy is presented by the Coulomb energy density—E_C = [flywheel kinetic energy/(sample area × normal stress)]—with units of meters (*9*) (tables S3 and S4).

We first consider a typical run, in which a SWG sample (#733, Fig. 2A) is sheared under normal stress σ_n = 6.8 MPa, and E_C = 0.42 m. The patch accelerated to peak velocity of V_p = 0.70 m/s in ~0.1 s and slipped for 0.86 m during 2.50 s. The initial patch strength (μ_s = 0.66) briefly increased (μ = 0.69) and then dropped to a minimum value of μ_{min} = 0.35. Finally, the patch strength recovered to μ = 0.81 as the patch decelerated (Fig. 2A).

Similar patterns of strength evolution were observed for ELSE experiments with the following characteristics (Fig. 2, A to D, and figs. S7 and S8): (i) The initial frictional strength (μ_s) was high and usually showed a brief strengthening stage. (ii) As slip continued, the strength decreased to a minimum value, μ_{min}, frequently followed by restrengthening during deceleration. (iii) Most ELSE runs (48 out of 66 experiments) displayed substantial dynamic weakening (*9*) that primarily depends on E_C (tables S3 and S4). Five runs with E_C < 0.001 m did not slip, four runs with E_C < 0.03 m slipped but did not reach weakening, and nine runs displayed negligible weakening. (iv) SWG samples loaded by E_C > 0.1 m displayed high-frequency stick-slip behavior; this mode was less common in KD samples. (v) The total slip distance, D, and the Coulomb energy density are related by $E_C = 0.605 \times D^{0.933}$ for both granite and dolomite experiments, over almost four orders of magnitude (Fig. 3A).

This strength evolution in ELSE runs is similar to strength evolution in earthquake models (Fig. 1C), stick-slip experiments (Fig. 1B), variable-rate experiments (*10*), and seismic analyses (Fig. 1D). To test this similarity, we assumed that the measured slip in ELSE experiments is equivalent to the average slip, $\overline{D}$, during an earthquake. Then, we used empirical relationships (*11*) between the moment magnitude (M_w) and $\overline{D}$, to find that ELSE (D = 0.003 to 4.6 m) corresponds to earthquakes in the range M_w = 4 to 8 (upper axis, Fig. 3A). Further, two other experimental parameters—peak velocity (1 m/s) and rise time (0.1 to 10 s) (Fig. 3A)—have values similar to the equivalent parameters of earthquakes (*2*). It appears that ELSE runs are similar to earthquakes in three ways: (i) a finite amount of stored energy; (ii) fault strength evolution pattern (Figs. 1D and 2); and (iii) seismically observed values, such as average slip, peak velocity and rise time (Fig. 3A). We propose that ELSE tests are experimental proxies for fault-patch behavior during earthquakes of M_w = 4 to 8 and now apply ELSE results to the questions of total earthquake energy and weakening distance (*9*).

To examine whether the experimental E_C is a reasonable estimate of the total earthquake energy, we compared experimental E_C to the breakdown (or fracture) energy (E_G) of six earthquakes (*2*) of M_w = 5.6 to 7.2 (*9*) (table S2). Breakdown energy is only a fraction of the total earthquake energy (*2*, *6*, *9*). As we did with our representation of E_C, we divide the seismic E_G by the corresponding σ_n (*9*), and the E_G/σ_n values are plotted with respect to their slip distance (vertical lines, Fig. 3A). Most (9 out of 11) of seismic E_G/σ_n values are small fractions (0.005 to 0.07) of the energy density of ELSE, as expected for

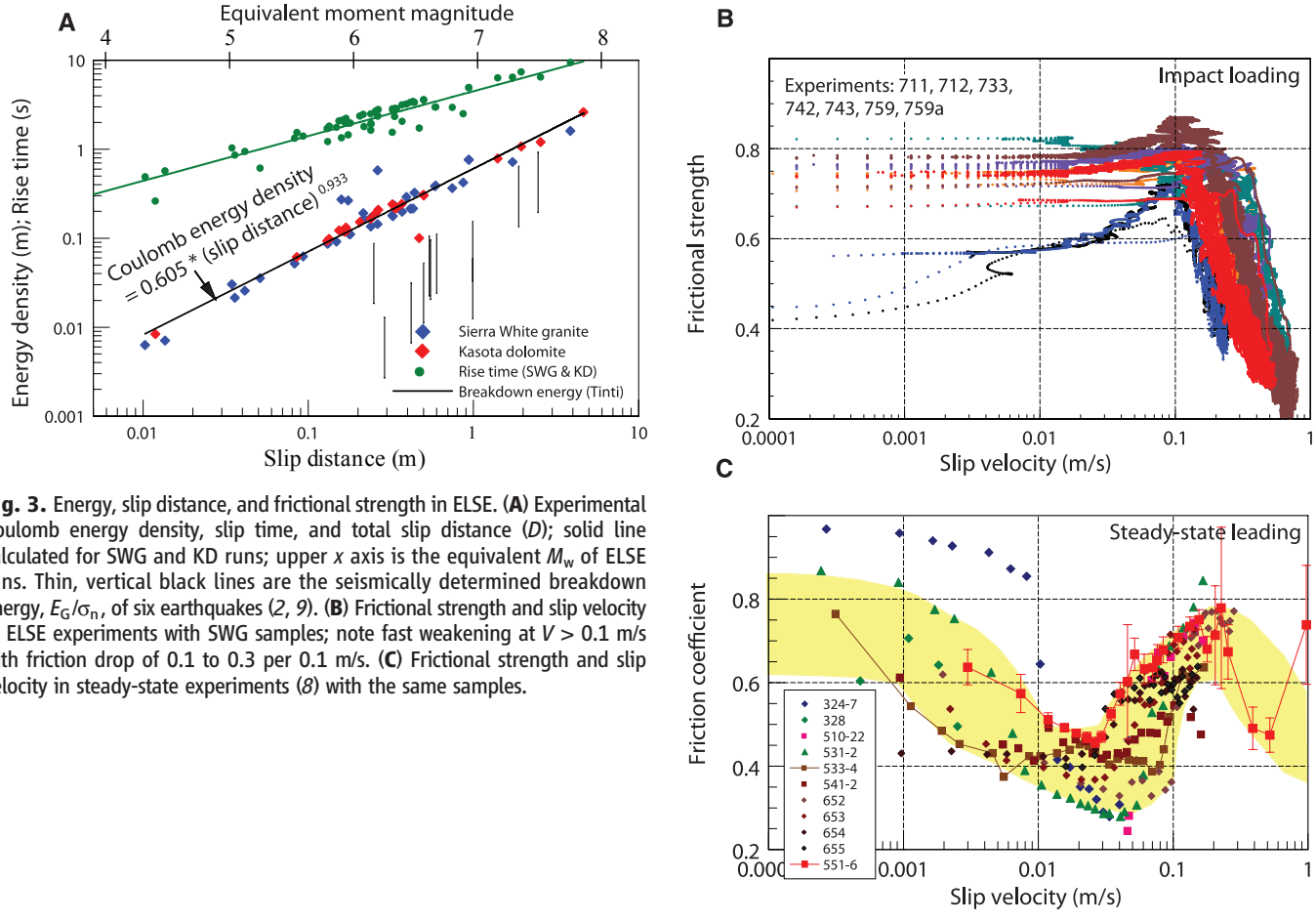

Fig. 3. Energy, slip distance, and frictional strength in ELSE. (**A**) Experimental Coulomb energy density, slip time, and total slip distance (D); solid line calculated for SWG and KD runs; upper x axis is the equivalent M_w of ELSE runs. Thin, vertical black lines are the seismically determined breakdown energy, E_G/σ_n, of six earthquakes (*2*, *9*). (**B**) Frictional strength and slip velocity in ELSE experiments with SWG samples; note fast weakening at V > 0.1 m/s with friction drop of 0.1 to 0.3 per 0.1 m/s. (**C**) Frictional strength and slip velocity in steady-state experiments (*8*) with the same samples.

fracture energy (*6*, *9*, *12*, *13*). The energy budget measured locally on a fault patch does not include radiated energy (*4*), and radiated energy is generally considered small compared with dissipated energy. We thus speculate that the experimental Coulomb energy density, $E_C = 0.605 \times D^{0.933}$, provides a reasonable estimate of total earthquake energy, a quantity that cannot be determined from seismic data (*2*, *4*).

We now consider slip-weakening distance, d_C, (Fig. 1, C and D). In friction experiments, d_C ranges from microns in direct shear (*3*, *6*, *7*) to meters in rotary shear (*8*, *10*, *14*, *15*). We identified d_C as the first slope break of the strength-displacement curve (Fig. 2, C and D). The 49 ELSE runs that display substantial dynamic weakening reveal d_C with mean values of 2.7 and 1.2 cm for SWG and KD, respectively. We attribute these d_C values, which are smaller than in most other rotary tests, to ELSE loading style. The fault patch in ELSE is abruptly loaded by engaging the spinning flywheel through a fast-acting clutch, and this impact loading profoundly affects the patch response. In ELSE runs with SWG samples (Fig. 3B), the frictional strength is 0.6 to 0.8 for $V < 0.1$ m/s, and it drops sharply to as low as $\mu \cong 0.2$ for $V > 0.1$ m/s. In contrast, our constant-velocity, steady-state experiments (*8*) (Fig. 3C) exhibit strikingly different friction-velocity relations. Because both sets of experiments were conducted on the same rock samples, the dissimilarity is attributed solely to the different loading mode, as already observed by (*10*). We further noted that fault strength and wear rate (*9*) evolve systematically with slip acceleration: A close correlation exists between the evolutions of acceleration (blue), strength (red), and wear rate (black) (Fig. 4 and figs. S7 and S8). In addition, dynamic weakening is restricted to the period of intense acceleration (up to 25 m/s^2 during ~0.1 s) (Fig. 4, A and B, and figs. S9 and S10), and d_C is reached within the initial acceleration spike.

The above relations of acceleration and weakening distance were previously observed in stick-slip (*3*) (Fig. 1B) and rotary-shear experiments (*9*, *10*, *16*, *17*) (fig. S5). The constitutive relations between acceleration, velocity, and critical distance were derived with the cohesive-zone model (*3*, *18*), which assumes that the extreme acceleration and stress at the tip of a propagating shear rupture leads to fault breakdown. ELSE results fit well the constitutive relations predicted by the cohesive-zone model (*9*) (Fig. 4C). Stick-slip and ELSE experiments (elastic versus kinetic energy) fit the same theoretical model, which suggests that the acceleration effect does not depend on details of the loading system.

What is the mechanism of cohesive-zone breakdown? Experimental stick-slip events (*3*) display intense acceleration (<4 km/s^2), which induces extreme strain rates (~10^4 s^{-1}) that increase rock brittleness and fragmentation (*19*, *20*). These processes temporarily intensify fault wear as manifested by high initial wear rates of 10^2 to 10^4 μm/m (Fig. 4 and figs. S9 and S10). This intense wear generates a layer of fine-grain powder (gouge) (*8*, *10*, *16*) that reduces the fault strength by powder lubrication (*8*, *14*, *20*, *21*). Thus, slip-acceleration speeds up fault wear and gouge formation and by doing so quickens weakening and shortens d_C. Yet, the accelerated weakening does not change the steady-state friction (*15*). Accelerated weakening is likely to be active in earthquakes where fault patches are accelerated by the rupture front (Fig. 4C).

It is generally accepted that earthquake dynamic weakening is determined by slip distance and slip velocity (*2*–*5*, *8*, *14*–*16*). We experimen-

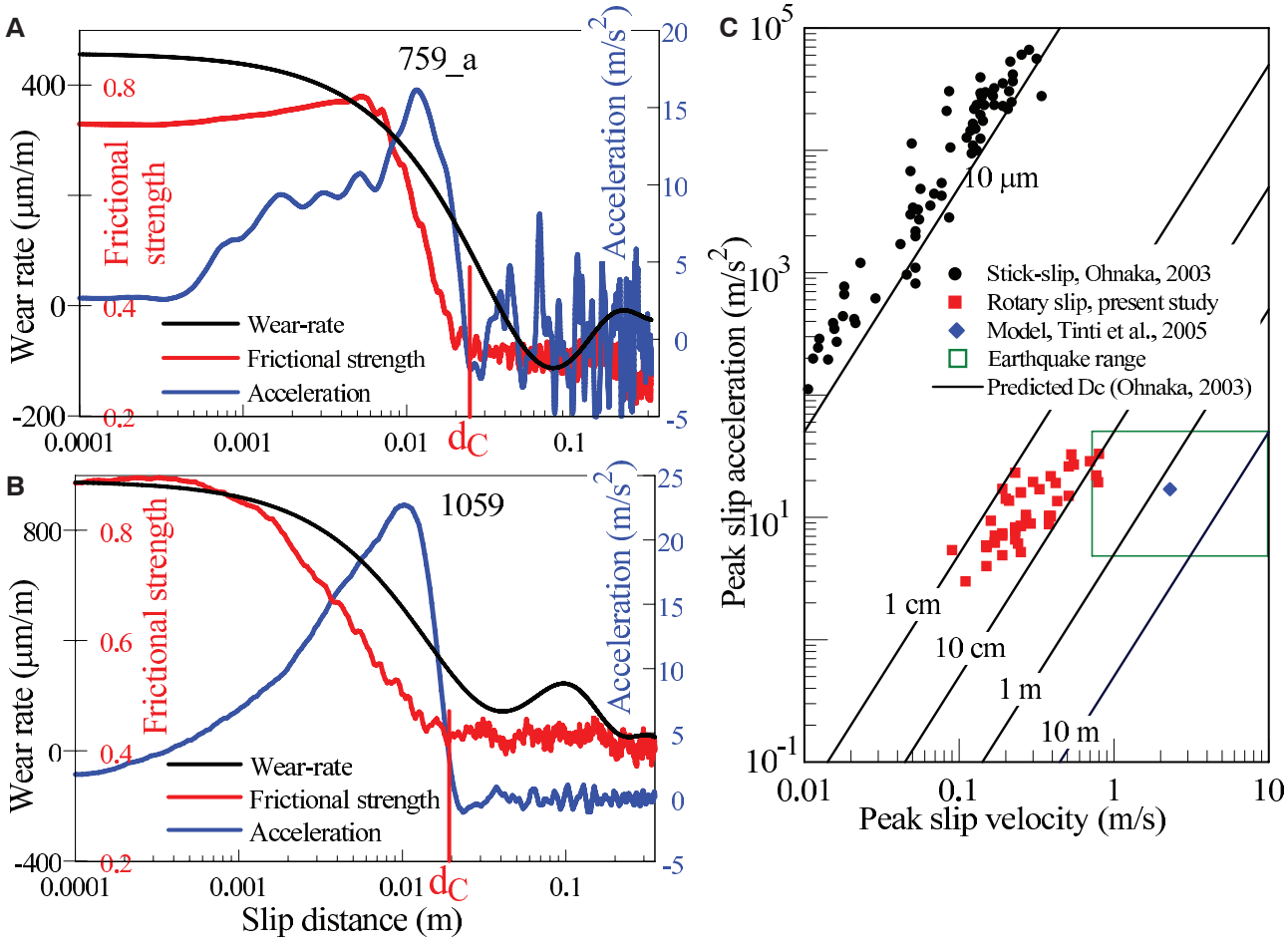

Fig. 4. Slip acceleration (blue), strength evolution (red), and fault wear rate (black) during the first 0.5 s of slip in SWG sample (**A**) and KD sample (**B**) (*9*). (**C**) Acceleration-velocity-d_C relations according to the cohesive-zone model (*3*, *9*). The inclined lines indicate the expected d_C (*9*); the projected ELSE data (red points) fall in the d_C = 1 to 10 cm range that fits the experimental range of d_C = 0.3 to 9.2 cm.

tally demonstrated that slip acceleration quickens fault weakening, and, in light of the transient nature of earthquake slip (*1*–*3*), we propose that slip acceleration controls seismic weakening in addition to slip distance and slip velocity.

References and Notes

1. T. H. Heaton, *Phys. Earth Planet. Inter.* **64**, 1 (1990).
2. E. Tinti, P. Spudich, M. Cocco, *J. Geophys. Res.* **110**, B12303 (2005).
3. M. Ohnaka, T. Yamashita, *J. Geophys. Res.* **94**, 4089 (1989).
4. H. Kanamori, L. Rivera, in *Earthquakes: Radiated Energy and the Physics of Faulting*, R. E. Abercrombie, A. McGarr, G. Di Toro, H. Kanamori, Eds. (AGU, Washington, DC, 2006), pp. 3–13.
5. D. J. Andrews, *J. Geophys. Res.* **110**, B01307 (2005).
6. D. A. Lockner, P. G. Okubo, *J. Geophys. Res.* **88**, 4313 (1983).
7. P. G. Okubo, J. H. Dieterich, *Geophys. Res. Lett.* **8**, 887 (1981).
8. Z. Reches, D. A. Lockner, *Nature* **467**, 452 (2010).
9. Materials and methods are available on *Science* Online.
10. H. Sone, T. Shimamoto, *Nat. Geosci.* **2**, 705 (2009).
11. D. L. Wells, K. J. Coppersmith, *Bull. Seismol. Soc. Am.* **84**, 974 (1994).
12. D. L. Olgaard, W. F. Brace, *Int. J. Rock Mech. Min. Sci.* **20**, 11 (1983).
13. B. Wilson, T. A. Dewers, Z. Reches, J. Brune, *Nature* **434**, 749 (2005).
14. R. Han, T. Hirose, T. Shimamoto, *J. Geophys. Res.* **115**, B03412 (2010).
15. A. Niemeijer, G. DiToro, S. Nielsen, F. Di Felice, *J. Geophys. Res.* **116**, B07404 (2011).
16. D. L. Goldsby, T. E. Tullis, *Science* **334**, 216 (2011).
17. E. Fukuyama, K. Mizoguchi, *Int. J. Fract.* **163**, 15 (2010).
18. M. Ohnaka, *J. Geophys. Res.* **108**, 2080 (2003).
19. D. E. Grady, M. E. Kipp, *J. Appl. Phys.* **58**, 1210 (1985).
20. Z. Reches, T. A. Dewers, *Earth Planet. Sci. Lett.* **235**, 361 (2005).
21. E. Y. A. Wornyoh, V. K. Jasti, C. F. Higgs III, *J. Tribol.* **129**, 438 (2007).

Acknowledgments: We thank J. Young, J. Fineberg, and E. Aharonov, and T. Shimamoto and two anonymous reviewers for their thoughtful reviews. This work was supported by NSF Geosciences awards 0732715 and 1045414 and NEHRP2011 award G11AP20008.

Supplementary Materials

www.sciencemag.org/cgi/content/full/338/6103/101/DC1
Materials and Methods
Supplementary Text
Figs. S1 to S10
Tables S1 to S4
References (*22*–*36*)

28 February 2012; accepted 14 August 2012
10.1126/science.1221195

The Efficacy of Student-Centered Instruction in Supporting Science Learning

E. M. Granger,[1]* T. H. Bevis,[1] Y. Saka,[2] S. A. Southerland,[3] V. Sampson,[3] R. L. Tate[4]

Transforming science learning through student-centered instruction that engages students in a variety of scientific practices is central to national science-teaching reform efforts. Our study employed a large-scale, randomized-cluster experimental design to compare the effects of student-centered and teacher-centered approaches on elementary school students' understanding of space-science concepts. Data included measures of student characteristics and learning and teacher characteristics and fidelity to the instructional approach. Results reveal that learning outcomes were higher for students enrolled in classrooms engaging in scientific practices through a student-centered approach; two moderators were identified. A statistical search for potential causal mechanisms for the observed outcomes uncovered two potential mediators: students' understanding of models and evidence and the self-efficacy of teachers.

The need for a different approach to science teaching and learning has been the focus of several recent policy and economic reports (*1*, *2*). Research as synthesized by the National Research Council suggests that the goal of science instruction should be to help students develop four aspects of scientific proficiency, the ability to (i) know, use, and interpret scientific explanations of the natural world; (ii) generate and evaluate scientific evidence and explanations; (iii) understand the nature and development of scientific knowledge; and (iv) participate productively in scientific practices and discourse (*3*–*5*). This approach to science teaching will require a shift from the teacher-centered instruction common in science classrooms to more student-centered methods of instruction. The defining feature of these instructional methods is who is doing the sense-making. In teacher-centered instruction, the sense-making is accomplished by the teacher and transmitted to students through lecture, textbooks, and confirmatory activities in which each step is specified by the teacher. In these classrooms, the instructional goal is to help students know scientific explanations, which is only part of the first aspect of scientific proficiency. In student-centered instruction, the sense-making rests with students, and the teacher acts as a facilitator to support the learning as students engage in scientific practices (*3*).

The effectiveness of student-centered instruction in helping students develop scientific proficiency is supported by a number of largely small-scale, narrowly focused studies (*3*, *5*). Despite accumulating support for a student-centered approach, few large-scale studies have evaluated the effectiveness of such instruction, and their results, taken as a whole, are contradictory and inconclusive (*6*–*13*). The same is true of only randomized-cluster or quasi-randomized studies examined separately (*6*, *11*, *14*, *15*). Many factors may contribute to the varied results, because tightly controlling potentially influential variables is difficult in classroom settings. One central factor is that the comparison condition (i.e., control group) is often "undefined or assumed to be 'traditional'" (*14*). Likewise, possible "contamination of the untreated teachers" and cases where investigators did not "vigorously guard" against special resource materials may have influenced results (*13*). Indeed, many studies described in the literature do not discuss how fidelity to the curriculum or instructional approach was measured or whether it was assessed.

We therefore compared the effectiveness of student-centered with teacher-centered instruction using a randomized-cluster experimental design, intended to control as many variables as possible given the inherent differences between the two instructional approaches. Specifically, the effectiveness of the student-centered Great Explorations in Math and Science Space Science Curriculum Sequence (SSCS) (*16*) and professional development of teachers focused on these materials (treatment group) was compared with that of a teacher-centered curriculum (district-adopted textbook) enacted with a teacher-centered approach (control group). For details of each curriculum, teacher professional development, and instructional approach, see the supplementary materials. Mindful of limits on securing meaningful data imposed by testing the age group for whom SSCS is appropriate (fourth and fifth grades), we selected four student outcomes aligned with the four aspects of scientific proficiency for this research: space science content knowledge, knowledge about models and evidence in science, views of scientific inquiry, and attitude toward science. The research was designed to (i) compare the effectiveness of the two instructional approaches in supporting elementary students' science learning; (ii) identify teacher characteristics (teacher moderating variables) that might influence the learning; (iii) identify those for whom this instructional approach might work (student moderating variables); and (iv) identify how the treatment might indirectly affect student outcomes (mediating variables).

[1]Office of Science Teaching Activities, Florida State University, Tallahassee, FL 32306–4295, USA. [2]Bülent Ecevit Üniversitesi Ereğli Eğitim Fakültesi, Turkey. [3]FSU-Teach/School of Teacher Education, Florida State University, Tallahassee, FL 32306–4459, USA. [4]Educational Evaluation and Research, Florida State University (retired), 415 Castleton Circle, Tallahassee, FL 32312, USA.

*To whom correspondence should be addressed: E-mail: granger@bio.fsu.edu

Supplementary Materials for

Rapid Acceleration Leads to Rapid Weakening in Earthquake-like Laboratory Experiments

Chang, JC, Lockner, DA, and Reches Z

correspondence to: reches@ou.edu

This PDF file includes:

Methods, Materials, and Experimental procedures
SupplementaryText
Figs. S1 to S10
Tables S1 to S4

Materials and Methods

Methods summary

The present experiments of earthquake-like-slip-events conducted on solid blocks of Sierra White granite and Kasota dolomite (supplied by ColdSprings, Texas). Each sample includes two cylindrical blocks of 101.6 mm diameter and 50.8 mm height. The upper, stationary block has a raised-ring structure with an inner-diameter of 63.2 mm, and outer-diameter of 82.3 mm (Fig. S1D, E). The blocks were pressed against each other along the raised ring. The granite blocks are held by epoxy to aluminum cylindrical grips, surface-ground and roughened with 600-grit SiC powder. Thermocouples were cemented into holes drilled 3 mm and 6 mm away from the sliding-surfaces (Fig. S1D). The normal stress, σ_n, was kept constant during a given experiment, ranging from 0.5 MPa to 7.0 MPa, with one case of 28 MPa.

Experimental set-up[1]

Our experimental system has several essential properties to study fault behavior during earthquakes: (1) Capability to apply normal stress up to 35 MPa, slip velocity of 0.001 to 2 m/s, fast rise to full velocity (<0.1 s), and unlimited slip distance; (2) Continuous slip velocity (no need for periodic slip reversal); (3) A ring design of the fault blocks with small velocity difference (14%) between the outer and inner diameters, eliminating the need for velocity corrections. Slip velocity was calculated for the mean diameter; and (4) High frequency, continuous monitoring of the experimental data, including normal load, shear load, slip velocity, displacement normal to the fault surface, and sample temperature.

Loading system

The apparatus frame is 1.8 m tall with two massive decks (Fig. S1A-C). The decks are connected to each other by four rectangle legs. The tested sample is placed between the two decks, and it is loaded by the rotary train from below and by normal stress from above (Fig. S1). The power system includes:

(1) A 100 HP three-phase electric motor (Reliance) and controller (Baldor) that provides torque of up to 3,000 Nm at any velocity from 0 RPM to 3300 RPM, and which can accelerate to full rotation speed in 0.1 sec. The motor velocity is monitored and controlled through an 8192 sector encoder.
(2) The main rotary shaft is powered by the motor with 1:6 velocity reduction sprockets.
(3) A 225 kg flywheel with its own clutch.
(4) An electromagnetic clutch (Ogura) with full engagement in 30 ms.
(5) A hydraulic piston system (Enerpac) with axial load up to 9,500 N.
(6) Torque monitoring system (Fig. S1A, B) designed to measure to shear stress along the experimental fault.

[1] Reference to commercial product names should not be construed as an endorsement. Rather, specific components are identified to provide reference for independent determination of machine performance.

Control system

The control system is based on National Instruments components, and it includes a SCXI-1100 with modules 1124 (analog control) 1161 (relay control), 1520 (load cell/strain gage), and 1600 (data acquisition and multiplexer), as well as a USB-6210 (sample encoder measurement). The system operations are control by a dedicated LabView (NI) program. Monitoring devices are described below.

Samples composition

Sierra White granite (SWG). The electron-microprobe (EMP) modal analysis shows that this rock is comprised of six main minerals: plagioclase (48%), quartz (38%), alkali-feldspar (5%), ferromagnesian- mica (5%), and muscovite (5%). Mean grain size is about 0.3 mm; mean void space in EMP images is ~4%.

Kasota dolomite (KD). The samples of Kasota dolomite were supplied by Cold Spring Granite, TX. It is quarried at Mankato, Minnesota, and it is supplied under the commercial name "Kasota Valley limestone". The XRD analysis indicates that our samples are 97.3% dolomite, 2.6% quartz and traces of plagioclase.

Experimental procedure

Loading

A key requirement in our earthquake simulation is that the time-histories of both friction and slip-velocity will be determined by the sample response and not programmed by the operator. To achieve this requirement, we utilize the massive (225 kg) flywheel of our system. The flywheel is linked to the power axis with two clutches. Clutch #1 connects/separates the flywheel to/from the motor; it is a "dog tooth" clutch that engages by four interlocking cogs on each side. It is engaged manually before the experiment, and disengaged by the controlling program during the experiment. Clutch #2 connects/separates the flywheel to/from the sample. It is an electromagnetic clutch that is fully engaged within 30 ms; it is engaged/disengaged by the controlling program.

The loading procedure during an ELSE run, which is only briefly described in the paper, is described here in full details in Table S1. The table also includes the assumed corresponding steps of the rupturing process of a fault patch during an earthquake. During a run, the clutches operate in the following sequence:

Step I (Table S1). Before the run, clutch #1 is engaged and clutch #2 is disengaged. This action guarantees no shear loading on the sample during the energy accumulation stage of the flywheel (Step II, Table S1).

Step II (Table S1). Early in the run, the flywheel is rotated by the motor to the selected speed while the condition of Step I is maintained, and thus no sliding occurs on the sample.

Step VI (Table S1). Clutch #1 is disengaged to disconnect the flywheel from the motor, and simultaneously clutch #2 is fully engaged. The flywheel continues to rotate by its own inertia, and transfers its kinetic energy to the sample through the engaged clutch #2 (Steps V-VII, Table S1).

Energy units

Only two controlling parameters were pre-selected for each experiment: the energy density E_T = (total flywheel kinetic energy/patch area), and the normal stress on the patch, σ_n. During slip, the flywheel energy is dissipated by patch frictional work; the latter equals $\bar{\mu}\sigma_n D$, where $\bar{\mu}$ is the average friction coefficient, and D is total slip. Thus, the ratio $E_C = E_T/\sigma_n \sim \bar{\mu} D$ is an energy parameter that controls total slip. We define E_C as 'Coulomb energy density' (with units of meters). In the present experiments, E_C ranges from $1.4 \cdot 10^{-6}$ to 2.6m (Table S1).

Data monitoring and analysis

Equipment

The monitored parameters are:

-Sample normal load is measured with Honeywell load-cell installed below the axial load piston.

-Sample torque is measured with a 1250 lbs load cell made by Transducer Techniques, which is installed against a 0.1524 m arm connected to the upper, stationary block.

-Displacement normal to the fault surface is measured with four eddy-current sensors made by Lion's Precision (± 1 micron accuracy).

-Sample temperature is measured with two K thermocouples (Omega) that are embedded 3 and 5 mm from the sliding surfaces (Fig. S1).

-Sample angular velocity is measured with a Sick-Stegmann encoder (4096 sections per revolution) installed below the lower, rotating block. Both the encoder counts and its voltage output were recorded.

-Motor velocity is measured with a second, identical Sick-Stegmann encoder installed on the motor.

-Motor torque is a voltage value output of the Baldor controller.

Data were recorded continuously at rate of either 5,000 sample/sec or 2,000 sample/sec.

Data filtering

The recorded data were checked and filtered as follows.

1. Checking and correcting time-lag between the two monitoring units of SCXI-1100 (all volt data output) and the USB-6210 (counter data from the sample-encoder). Checking was done by comparing the timing between the encoder counting recorded on the USB-6210, and the encoder voltage recorded with the SCXI-1100, and the time-lag was corrected by shifting the time difference.
2. Slip-velocity was calculated in steps. First fitting piece-wise polynomial curves (typically power of 10-20) to the encoder counter data. This operation smoothen the step-wise output of the encoder and eliminated artifacts of temporary velocity jumps (associated with the width of sections within the encoder). The velocity is then calculated from this fitted curve according to sample geometry.
3. Acceleration was calculated as the derivative of the velocity history, and filtered with an average-running-window of 0.01 s width.
4. Friction coefficient (=frictional strength), μ, is the calculated ratio of shear load (measured by the torque load cell) to normal load (measured by the axial load cell). The friction coefficient is filtered with an average-running-window of 0.01 s width.

Wear measurement and wear-rate calculations

The common methods of wear measurements are (1) weighing wear products; (2) measuring displacement normal to the sliding surfaces; and (3) optical techniques. The weighing powder method is a time-consuming process that disrupts the structure of the fault, and thus makes it impossible to return to the previous stage after the measurement. Optical methods cannot be conducted continuously, and require an accurate reference surface. We determine wear by continuously monitoring the fault-normal-displacement, U, with four eddy-current sensors (~1 μm accuracy) attached to the sample holders. Positive U is defined as closure across the fault, and negative U as fault dilation. The closure has four contributions: (1) Surface wear, W, indicated by fault closure (U > 0); (2) Thermal expansion (U < 0) due to frictional heating of the sample; (3) Compaction (U > 0) or dilation (U < 0) of the gouge zone or the sample; and (4) elastic response of changes in the normal stress.

We calculated the time-dependent wear-rate in steps. First, the thermal contribution is determined by using the measured temperature from the thermocouple embedded 3 mm from the fault. The fault closure due to its cooling was monitored for a period of 10-120 s after the sample stopped slipping. During this period of post slipping, the fault closure is nearly linear with the decrease in temperature, and this closure is used to calculated an empirical thermal closure-rate parameter, $T_G = dU/dT$, where T is the measured temperature during the cooling period. This coefficient varies between runs in the range of 0.2 to 1.6 micron/°C. The thermal contribution during slip is $\Delta U_T = T_G \cdot \Delta T$ where ΔT is the increase in temperature as measured with the same thermocouple used to calculate T_G. The value of ΔU_T is subtracted from the measure closure to obtain the thermally adjusted U_t. Once the gouge layer is established along the patch surface, its thickness is probably nearly constant as the excess gouge is free to be ejected from the sliding surface. Under this condition, the fault-wear is approximately equal to the thermally adjusted closure, $W \approx U_t$. Thus, this wear is the thermally corrected closure (in μm). Next, we corrected for the elastic response of the sample due to normal stress changes. The normal load is maintained constant by an air-pressure/oil actuator that controls the oil pressure in the loading hydraulic piston; this system displays typical short-term variations of 5-10%. We independently measured the elastic fault-normal displacement by using the eddy current sensors under a range of normal loads, and then used the displacement-load relations to correct for U_t during slip. Finally, we fit a polynomial curve (order of 5-13) to the wear data, and take the derivative of this fitted-curve with respect to fault-slip to obtain the dimensionless *wear-rate*, $WR = (dW/dx)$, where x is fault-parallel slip.

There is no universal wear-rate unit, and we used a simple, pure geometric unit,

$$WR \equiv \frac{[volume\ of\ wear\ products]/[area\ of\ sliding\ surfaces]}{[slip\ distance]} \equiv \frac{[thermally\ corrected\ closure]}{[slip\ distance]}$$

The wear-rate unit can be dimensionless [m/m], or [10^{-6} m/m] = [μm/m]; we used the latter, which is more suitable for the range of our experimental results.

Supplementary Text

Supplementary experimental observations

Average frictional coefficient

Dynamic fault weakening to a minimum-strength, μ_{min}, is commonly regarded as the source of earthquake slip instability (8). However, μ_{min} is a transient property (Figs. 1C, D, 2A, C, S5, S6), and thus cannot represent fault strength during the entire slip event. Further, μ_{min} is not attained at a consistent displacement in different slip events (2) (Figs. 1C, D, 2A-D, S5, S6). We propose that the 'average frictional strength', $\overline{\mu}$, is a more relevant indicator of the dynamic-strength of the fault. In ELSE experiments, the average strength values (Fig. S2) have simple relations to the total slip, $\overline{\mu} = 0.77 - 0.16 \cdot D^{0.46}$. This relationship indicates that during slip, average frictional strength decreases with increasing displacement (and energy density). Thus, if the strength-distance relations of Figure S2 are applicable to earthquakes, they can explain the better slip efficiency of large earthquakes.

Application to earthquakes data

The paper discuss the total energy in ELSE experiments and compare it to the fracture energy, E_G, that was determined from seismic data. We used the seismic analysis of (2) who calculated the fracture energy associated with recent earthquakes in the moment-magnitude range of M_W = 5.6-7.2. They used slip- and velocity-histories of multiple sub-faults as determined from the inversion of strong ground motion, and applied crustal elastic properties to calculate (finite difference) the dynamic traction history for each of the sub-faults. The total earthquake work cannot be calculated from seismic data (2, 4), and Tinti et al. (2005) (2) assumed an arbitrarily high ambient traction. They calculated the fracture energy (4), E_G, (which they defined as 'breakdown work') as the surplus work done above the minimum shear traction, μ_{min}, in their shear traction curves (Fig. 1C). Note that the minimum frictional strength of (2) is defined similarly to μ_{min}, in our analysis. The breakdown work (=fracture work), $W_b = E_G$, is the integrated value of [shear stress · slip velocity. The calculated breakdown work ranged $4 \cdot 10^5$ to $2 \cdot 10^7$ J/m^2 for analyzed earthquakes (2) (Table S2).

Our analysis indicates that the experimental slip, D, during an ELSE experiment, is proportional to the Coulomb energy density, $E_C = 0.605 \cdot D^{0.933}$, for both granite and dolomite experiments (Fig. 3A). The seismic E_G of Tinti et al. (2005) has to be divided by the relevant normal stress on the fault as the Coulomb energy density, $E_C = E_T/\sigma_n$, better represents the total energy for ELSE experiments. To calculate the σ_n in (2) analysis, we first assumed that the analyzed faults are vertical, and that the normal stress on them is controlled by the overburden weight of the rock column (we note that the normal stress on a strike-slip fault may differ from the overburden load). Then, the earthquakes mean depth, h, is used to estimate the normal stress, σ_n, with two bounds (Table S2). The upper bound is σ_{nU} = [rock overburden pressure – groundwater pressure]

$= (\rho_{rock} - \rho_{water})\cdot g\cdot h$, where ρ_{rock} and ρ_{water} are the density of crustal rocks and water, respectively, and g is gravitational acceleration. The lower bound, σ_{nL} is based on the Poisson's effect in which only part of the overburden is converted to normal stress on vertical plane, and $\sigma_{nL} = \sigma_{nU}\cdot(\nu/1-\nu)$ where ν is the Poisson's ratio. We plotted the ratios E_G/σ_{nU} and E_G/σ_{nL} (Table S2), as the fracture energy ratio E_G/σ_n as vertical black lines in Fig. 3A.

Fracture (=breakdown) energy component of total earthquake energy

It is generally viewed that earthquake energy, E_T, is dissipated by three main components (22, 23),

$$E_T = E_G + E_H + E_R$$

where E_G is the fracture energy required to break down the locked fault, E_H is the frictional heat energy to maintain slip, and E_R is the radiation energy. It is also generally accepted that E_R is only 5-6% of E_T (22). Thus, the major part of the energy is dissipated by the first two energy terms in the above equation (Fig. 1C). While E_R and E_G can be estimated from seismic analyses (2, 4), the magnitude of E_H, and as a result the magnitude of E_T, cannot be determined from seismic data (23). Following the concept of Griffith, it is envisioned that the fracture energy E_G is the energy dissipated by new surface area that forms during the earthquake by pulverization and fracturing. There is however, a disagreement on the relative magnitude of the fracture energy E_G/E_H, and the estimate of this ratio range from ~ 0.001 (12, 24) to ~ 0.5 (13). The disagreement about relative size of the fracture energy (E_G/E_H) stems from (A) difficulty to assess the surface area of the fine-grain gouge; and (B) difficulty to evaluate the volume of the gouge that is formed during a single earthquake.

The surface area of the gouge can be evaluated by particle size distribution (PSD), by surface area measurement in the BET method, or by combination of the two methods (13). While these methods provide good results for granular materials with grain-size larger than a few microns, the results are problematic for fine powder with sub-micron to nanometer scale. The PSD analysis typically considers the surface area of smooth spheres, which may be reasonable approximation for abraded, coarse sand grains, but fails to describe more complex geometry of freshly fractured gouge powder (Fig. S3A). The more severe limitation is the tendency of ultra-fine grain powders to aggregate and sinter due to their large surface area (Fig. S3B, C). These processes were discussed in detailed by (25), may increase the apparent grains, and particularly eliminate the very fine grains with the large surface area. Wilson et al., measured PSD of fault gouge after tens of hours of continuous circulation, and found that the PSD becomes finer with time of circulation. They attributed this fining of the PSD to breaking of aggregates into the intrinsic building grains. They also found that the gouge powder from the San Andreas fault zone and from a small fault in a gold mine in South Africa have similar PSD with average grain size of ~ 0.25 μm. . Further, the TEM dark field method (25) on the same gouge powder indicated that apparently coherent grains of a few microns in size are composed of tens of smaller grains agglomerated together. The ultra-fine grains of Wilson's PSD implied very large surface area, approaching 100 m^2/gr, and relatively high fracture energy with E_G/E_H ~0.5.

These results of (13) were disputed by (26) who applied several circulation speeds on the same gouge from the San Andreas fault. They found that the PSD observed by (13) is reproducible under low circulation speed, but the PSD under high circulation speed shows almost no change with respect to the initial PSD. They suggested that grain settling at low circulation speed biased of (13) toward finer PSD, and thus exaggerated value of fracture energy.

Two recent experimental studies (27, 28) employed the BET method to evaluate the fracture energy associated with slip at high velocity. In experiments that used quartz grains (27), the BET results indicate that energy dissipated on grain crushing is only 0.0002-0.01 of frictional work. In experiments that used natural gouge from the Nojima fault (28), the BET results showed that surface area reduction with increasing velocity, and the SEM observations revealed that this reduction is heat induced welding of the fine grains.

With regard to the present analysis, Fig. 3A displays the 11 ratios of E_G / σ_{nL} for the six analyzed earthquakes that are listed in Table S2 (some of the earthquakes have more than one solution, 2). We found that 9 out of the 11 values show that E_G / σ_{nL} are 0.005-0.07 of E_C; these values fits previous laboratory analyses which suggest that fracture energy is very small fraction of friction energy (6, 12, 26-28). The two values of Landers earthquake (Table S2) are much higher with E_G / σ_{nL} = 0.25-0.36 E_C.

Comparison between ELSE loading and earthquake loading

Is the ELSE approach a reasonable simulation of fault-patch behavior during large earthquakes? There are several similarities and some limitations.

Energy magnitude. In both ELSE experiments and earthquakes the available energy is finite. In this respect, ELSE experiments differ from typical rotary shear experiments (8, 14, 15) in which the operator specifies the velocity history and run duration, and the motor supplies all the required energy regardless of the sample strength evolution.

Loading mode. In ELSE runs, the flywheel loads abruptly the fault patch, and it slows down almost linearly in time (Fig. 2). The loading history of a fault patch during an earthquake is unknown, and some of the theoretically proposed loading histories are similar to the loading history in ELSE. For example, cases f2, f3 and f4 in Fig. S4 (29), and the stress, velocity and strength model for a propagation slip pulse (Fig. 11 in 1). These models infer that the fault patch is quickly loaded to maximum velocity by the stress concentration at the tip of the earthquake front.

In ELSE experiments the energy drops linearly with time by the slowing flywheel. This is not always necesarily the case in an earthquake. If the earthquake slip grows in the ideal crack mode, than with increasing crack length, a larger volume of the wall rock can release elastic strain energy, and the available energy may increase during seismic rupture propagation. If the earthquake slip grows in the ideal slip-pulse mode (1), the pulse sweeps along the fault while drawing elastic strain energy from approximately constant volume, and thus the energy is likely to drop in time. In ELSE experiments the energy consistently decays and it fits better the second mode.

Energy magnitude and slip velocity. In ELSE experiments the energy is directly related to the flywheel velocity, and thus the peak-velocity of the experimental patch is

directly linked to the energy intensity. In earthquakes however, the slip-velocity has a non-trivial relationship to the released elastic energy (5). Simulating the latter condition was achieved in stick-slip experiments (3, 6, 7); however, those experiments were limited to very small slip, equivalent to $M_w < -5$. These slip events may simulate earthquake nucleation, but fall short of the mechanical power (30) and slip-magnitude of larger earthquakes. Currently, the ELSE approach is the only method to experimentally simulate large earthquakes.

Slip-acceleration and fault-weakening

Comparison with previous experiments

The ELSE observations of temporal association between acceleration spike and fault-weakening (Fig. 4) are not unique. Similar associations were reported in stick-slip (3) (Fig. 1B), rotary shear (15, 16) (Fig. S5) and impact shear experiments (31). These studies greatly differ from each other in type of apparatus, slip distance (μm to m), normal stress (a few to thousands of MPa), acceleration intensity (a few m/s^2 to km/s^2), and slip-velocities (0.01 to 40 m/s). The outstanding commonality is intense slip acceleration.

We examine here three recent cases of high-velocity, rotary shear experiments (Fig. S5). Niemeijer et al (15) kindly provided the raw data for their experiment s049 (Fig. 5 in 15) that was conducted on a gabbro sample under σ_n = 20 MPa and slip velocity of 3.0 m/s. The first 0.5 s of this experiment (Fig. S5A) shows an acceleration spike (blue) that lasted ~0.1 s with peak acceleration of ~ 50 m/s^2, and complex evolution of the frictional strength (red). One can recognize an early weakening stage when the friction coefficient dropped to $\mu \sim 0.1$ during the first 0.025 s (d_C ~ 5 mm, upper axis). This stage is followed by three cycles of strengthening-weakening until the steady-state stage is established at about 0.5 s. Previous high-velocity, shear experiments of gabbro samples also displayed two (or more) strengthening-weakening stages (32). The temporal strengthening was attributed to the high shear resistance of partial melt gouge, and the final weakening stage was explained by full-scale melt of gabbro blocks (15, 32, 33). Niemeijer et al (15) explained the three strengthening-weakening oscillations as partly "….induced by the energy input from the motor (in some experiments, the sample accelerates from 0 to 3000 rpm in 0.1 s, which is almost like hammering the sample)…" Further, the intense loading in experiment s049 of (15) was preceded by long, *insitu* grinding stage under low velocity that generated a layer of reddish-brown gouge which fully covered the gabbro fault surfaces (Fig. 4 in 15). This description of the intense loading (15) perfectly fits the impact applied by the flywheel in ELSE experiments and we postulate that the effect on the experimental fault was similar: abrupt, fast weakening. We interpret the first weakening with d_C ~ 5 mm in Fig. S5A as caused by lubrication within the already existing gouge layer (Fig. 4 in 15), similarly to ELSE experiments. According to our interpretation, the two weakening stages reflect different mechanisms, early powder lubrication with short d_C, and later melt weakening with long d_C. As our granite and dolomite samples did not melt, they display only the first weakening stage. We think that the two mechanisms, acceleration controlled powder lubrication and the thermally controlled melt weakening, are separated in time/distance and are probably independent

of each other. It is thus expected that both the intensity of melt weakening and its d_C do not depend on the initial acceleration, as indeed was found by Niemeijer et al. (15).

Another case of high-velocity, rotary-shear experiments were recently conducted on quartzite samples (16); here, the acceleration approached 40 m/s^2, and the slip-velocity was up to 0.36 m/s. Fig. S5B, which uses the Supplemental data of (16), also reveals similar acceleration-weakening relations to ELSE experiments, and similar friction-velocity relations (compare Fig. S5B with Figs. 4A). Goldsby and Tullis (16) attributed their results to 'flash heating' at highly stressed contacting asperities, and found good fit between experimental observations and flash heating predictions. These authors also found "...that a very thin layer of gouge [≤30 μm thick] formed on the initially bare rock surface." We propose a different interpretation for these experiments. First, the ≤30 μm gouge thickness indicates an intense, average wear-rate of ≤700 μm/m, during the 43 mm of slip; we suspect that the wear-rate was much higher during the initial slip-acceleration (Fig. 4). Second, a ≤30 μm thick gouge layer would cover the initially contacting asperities along the bare surface, and thus strongly reduce their extreme high stress. Third, the fault slip was probably accommodated within the newly-formed gouge layer, and not by shear between contacting asperities. We think that our model of the acceleration-driven wear-rate and associated powder-weakening better explains the observations of (16). Tisato et al. (34) tested limestone samples under similar conditions to (16), and their results (Fig. S5C) display similar patterns of acceleration-weakening to (16) [note that the acceleration stage in Fig. S5C is preceded by slip under very low velocity to a distance of 10 mm].

Acceleration control of fault weakening

The effect of acceleration of fault weakening was primarily examined in studies of shear rupture propagation. It was assumed that the slip along a propagating shear rupture increases the shear stress close to the tip, and this loading leads to strength degradation and breakdown of a cohesive zone ahead of the slipping area (Fig. S6A after 3). This breakdown facilitates the rupture propagation, and the dissipated energy is equivalent to 'fracture energy' or 'breakdown energy' in fracture mechanics. For a given fault patch, it is envisioned that the elevated shear stress and the breakdown energy are characteristics of the early stage of the patch slip (Figs. 1B, C, S6) (3, 18). Most experiments show that the breakdown stage is associated with a spike of intense acceleration that quickly decays (3, 18) (Figs. 4A, B, S6). Based on these observations in stick-slip experiments, Ohnaka and Yamashita (1989) developed the cohesive-zone model (Fig. S6A, B) in which stress, velocity and acceleration are in a transitional state with intense temporal variations (Fig. S6B). The results of two ELSE experiments are plotted (Fig. S6C, D) next to the idealized behavior of the cohesive-zone model (Fig S6B). Note that the displacement axes in Fig. S6C, D are in log scale to expand the early slip stage in experiments of large displacement. One may recognize that the transitional character of the stress, velocity and acceleration in ELSE (Fig. S6C, D) appear to generally fit the cohesive-zone concept of Ohnaka (Fig. S6C, D). In particular, ELSE curves display distinct spikes of velocity and acceleration, a short or no steady-state stage, and a slight strengthening during slip initiation (Fig. 4A, B, S6C, D).

Ohnaka and Yamashita (3) recognized the transient nature of the rupture process, and derived the relations between peak-slip-acceleration and peak-slip-velocity of the cohesive-zone model. They found that

$$(\text{peak-slip-acceleration}) = (h/d_C) \cdot (\text{peak-slip-velocity})^2$$

where d_C is the critical slip distance, and h is a constant which approximately equals 5. The plot of the peak values of acceleration and velocity in ELSE experiments (Fig. 4C) reveal that they are scattered in the predicted range of d_C = 1-10 cm of the above equation, which is in very good agreement with the experimentally observed d_C. Ohnaka (2003) (18) further proposed that the above equation is also valid to crustal earthquakes (Fig. 14 in 14) for which the peak velocity is larger than in his stick-slip experiments and the peak acceleration is significantly lower (Fig. 4C). We think that the cohesive-zone model outlines well the parametric relations in ELSE experiments that are placed close to the earthquake field (Fig. 4C).

Why small earthquakes are similar to large one?

We proposed in the paper that accelerated weakening is likely to be active in natural earthquakes in which fault-patches are intensely accelerated by the passing rupture front, and steady-state friction is not likely to be achieved (8). Weakening acceleration can explain some puzzling observations. For example, tiny earthquakes (M_w= -2.5 to -3.4) that were recorded in deep gold mines (35, 36) have the seismic signature of large earthquakes. However, with only tens of microns slip, these earthquakes cannot reach the typical seismic d_C (2). On the other hand, if the local acceleration was very high, the associated d_c can be on the order of few microns as suggested by the extreme acceleration of ~ 5 km/s^2 and d_C =1-2 μm in the stick-slip experiment in Fig. 1B (3).

Expanded data presentation

The results of a few typical experiments were presented in the paper, and here the data presentation is expanded. First, we list the main parameters of all ELSE experiments with Sierra While granite (Table S3) and Kasota dolomite (Table S4). The tables include the pre-selected conditions for each experiment: normal stress (= axial load), the 'Coulomb energy density', E_T/σ_n, and the maximum slip velocity. Both last two parameters depend on the selected angular velocity, ω, of the flywheel where the kinetic energy, E_T, is proportional to ω^2, and the slip velocity is linearly proportional to ω. The other parameters were determined from the experimental results. The tables also indicate the experiments that did not slip or did not weaken (total of 17 runs). The main reason for these behaviors is that the Coulomb energy density was too low to activate instability.

Second, in addition to the four experiments in the paper (Figs. 2C, D), we present here plots of the frictional strength and slip-velocity evolution, as functions of slip-distance for 12 experiments with Sierra White granite (Fig. S7), and 12 experiments with Kasota dolomite (Fig. S8). We also present plots of slip-acceleration, frictional strength, and wear-rates with respect to distance for 22 weakening experiments of Sierra White granite (Fig. S9), and 24 experiments with Kasota dolomite (Fig. S10) (in addition to the experiments in the paper Figs. 4A, B). Experiments with no slip or with negligible weakening are not plotted.

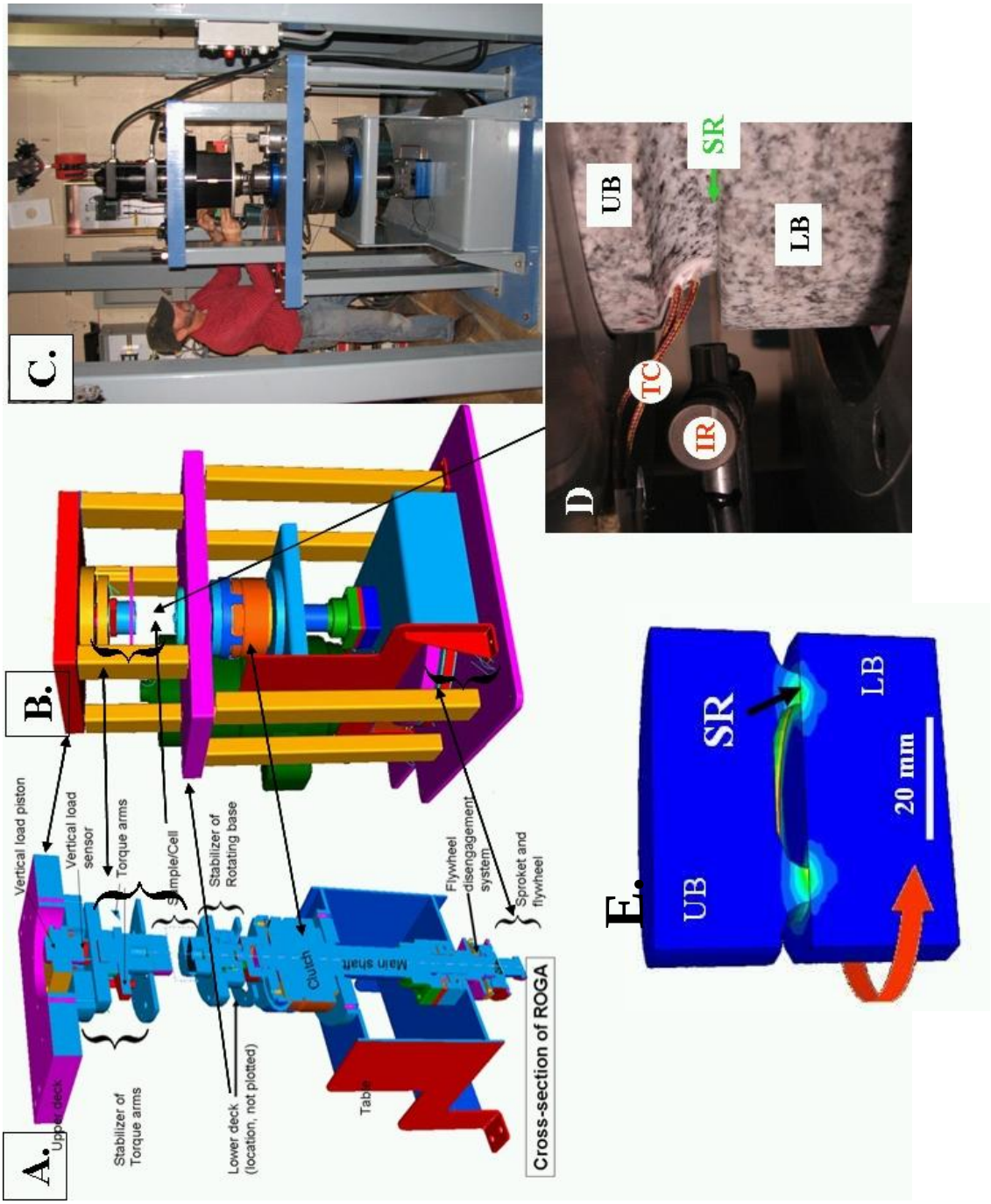

Fig. S1.

The rotary shear apparatus. A. Generalized cross section displaying power train. B. 3D view of the assembled apparatus. C. The apparatus with builder Joel Young. D. Sample blocks assembled in the loading frame. LB-lower block; UB-upper block; SR-sliding ring; TC-thermocouple wires; IR-infra red sensor. E. Sample design shown as vertical cut-through of two cylindrical blocks of solid granite rock. The colors indicate temperature distribution due to frictional heating calculated using a finite-element model.

.

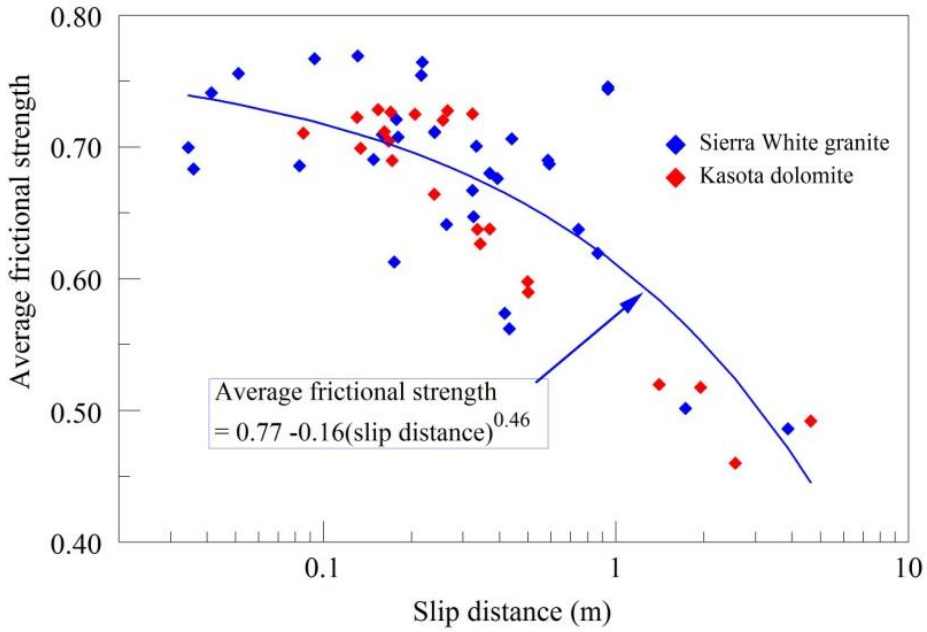

Fig. S2

Average frictional strength as function of total slip-distance the 57 ELSE runs with slip > 0.02 m.

.

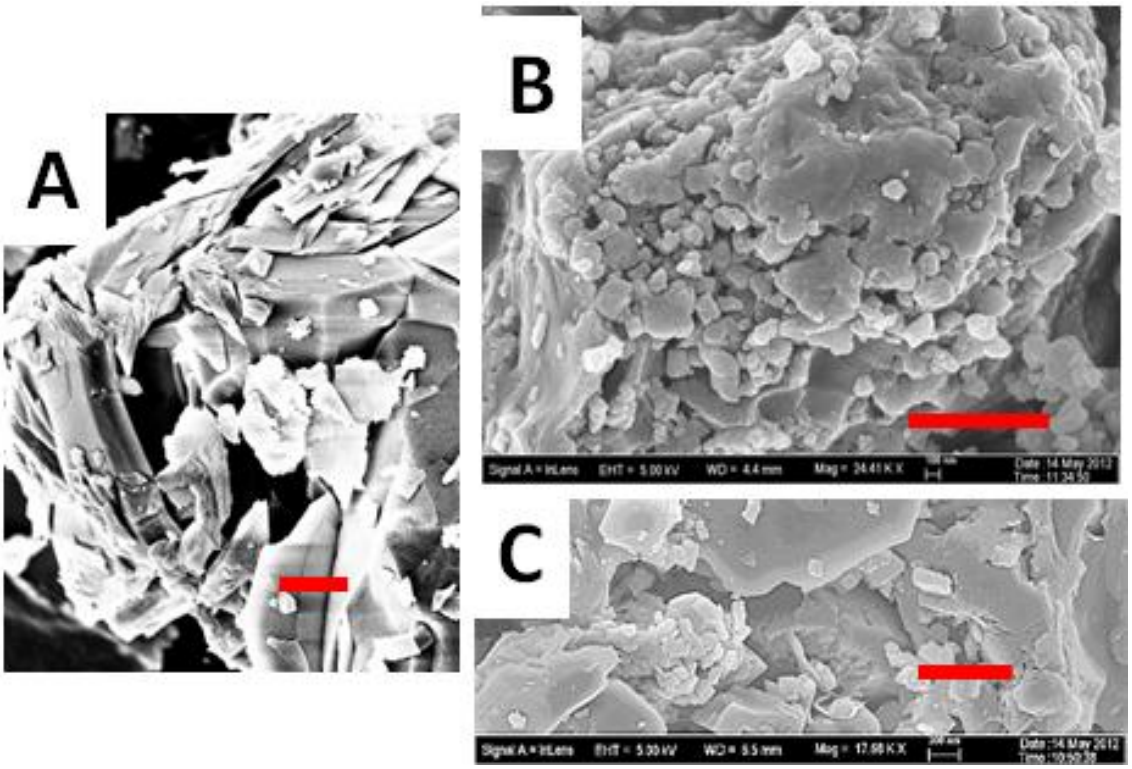

Fig. S3

SEM images of gouge powders; red scale bars are 1 micron long. A. Aggregate of angular quartz grains in fine grain gouge formed during a M =3.7 earthquake in a South African mine. B. Experimental gouge of Sierra White granite in the present experiments showing aggregation of sub-micron grains. C. Micron and sub-micron size grains in San Andreas fault-zone, Tejon Pass, California (13).

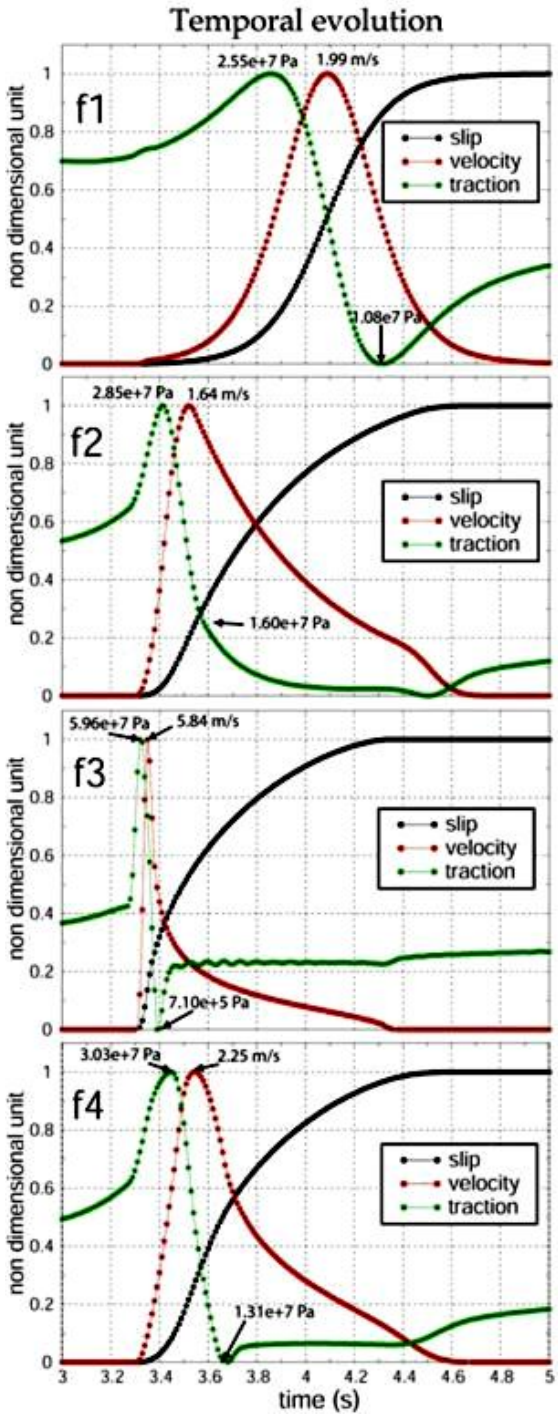

Fig. S4

Normalized time histories of slip (black), slip velocity (red), and dynamic traction (green) of theoretical consideration (29). Note the general similarity between cases f2, f3 and f4 and ELSE velocity and strength evolution (Fig. 2).

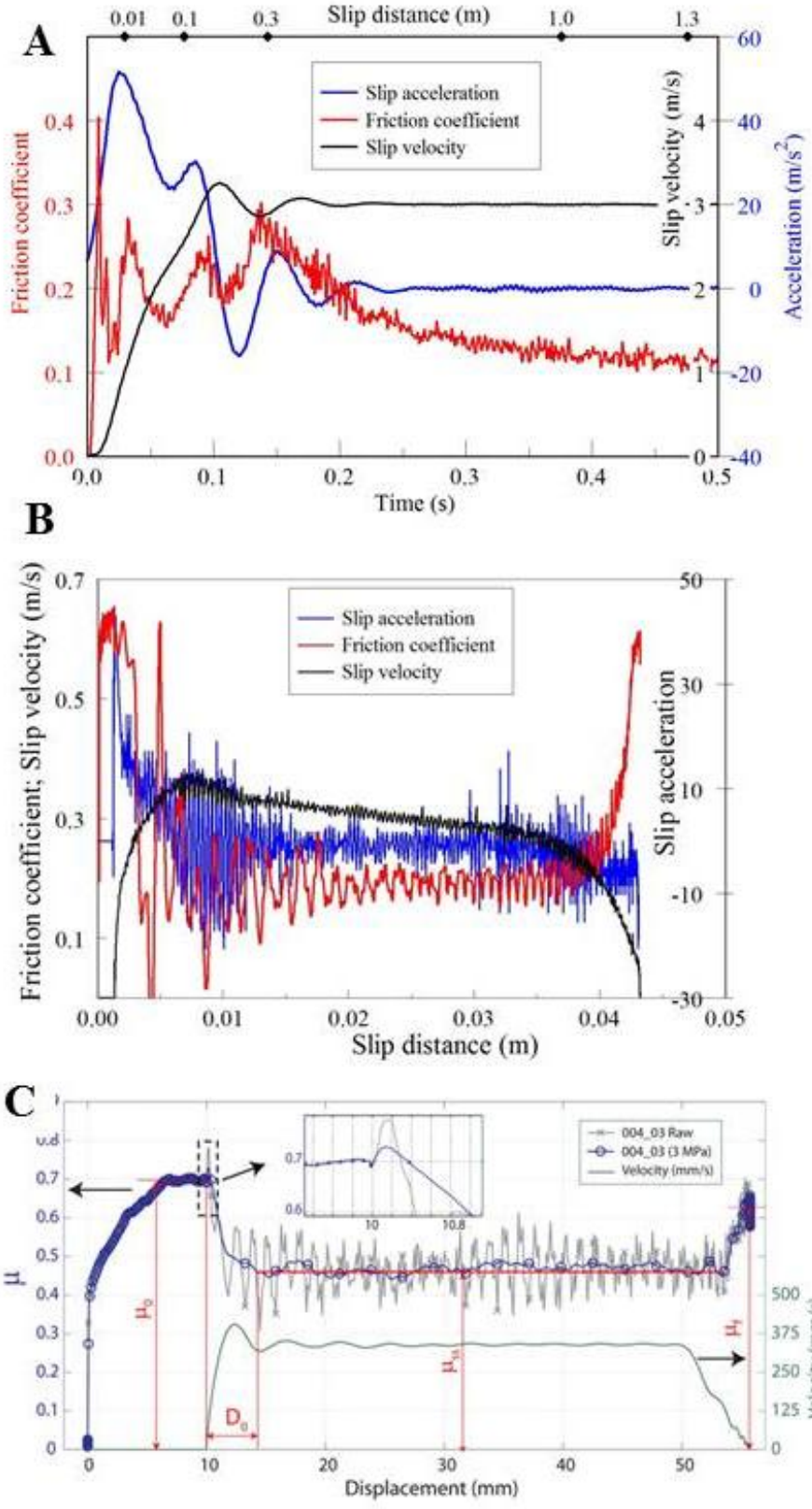
A
Slip distance (m)
0.01
0.1
0.3
1.0
1.3
Slip acceleration
Friction coefficient
Slip velocity
Friction coefficient
Slip velocity (m/s)
Acceleration (m/s²)
Time (s)
B
Friction coefficient; Slip velocity (m/s)
Slip acceleration
Slip distance (m)
C
004_03 Raw
004_03 (3 MPa)
Velocity (mm/s)
μ
Displacement (mm)
Velocity (mm/s)

Fig. S5

Velocity, acceleration and strength relations in rotary shear experiments. A. High velocity shear along a gabbro sample (data kindly provided by 15). Note that the initial weakening stages are associated with intense acceleration. B. Velocity, acceleration and strength relations of quartzite sample (plotted from supplementary data of 16). C. Velocity and strength relations of limestone sample (34); note d_C ~ 4 mm overlapping the acceleration stage.

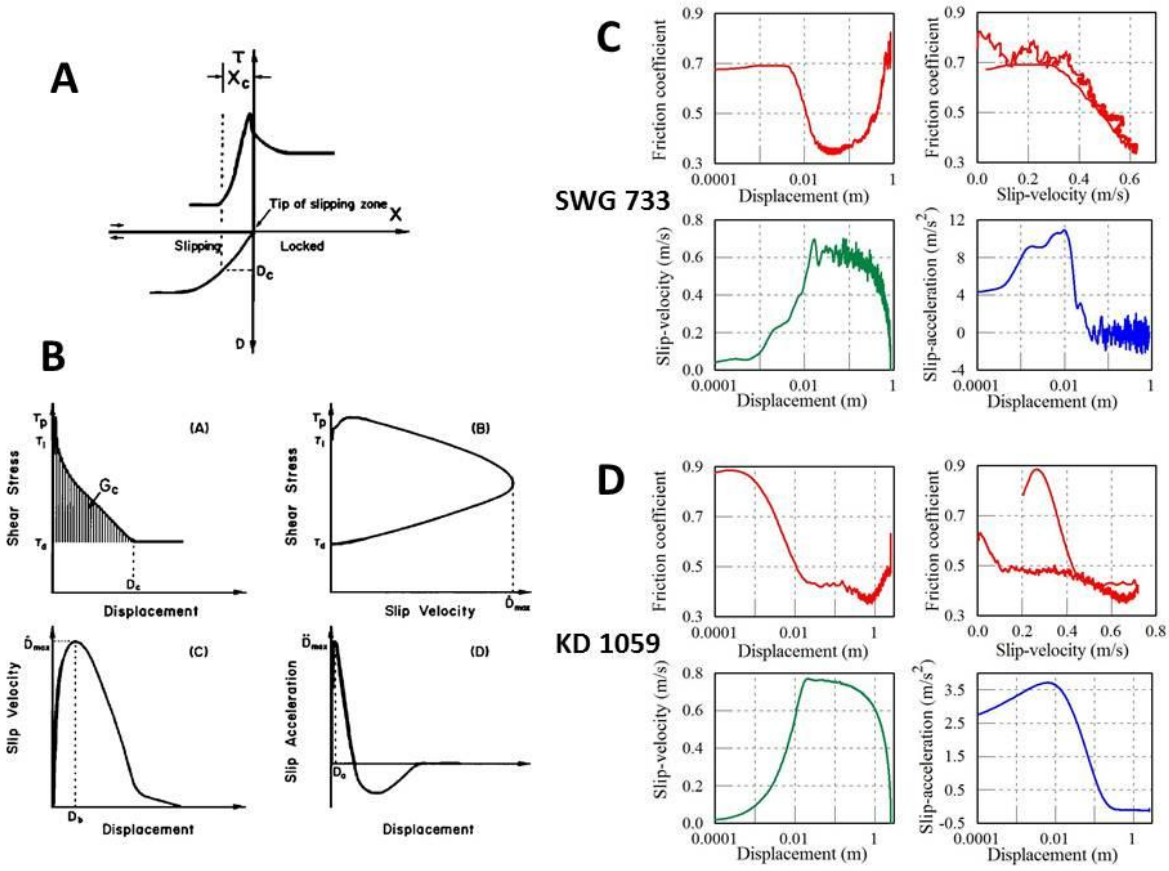

Fig. S6

A constitutive relations of the cohesive-zone model (3, 18). A. The conditions near the tip of a dynamically propagating shaer fracture during the cohesive zone breakdown. B. Idealized evolution of shear stress, velocity and acceleration and their relation to the displacement. Note that peak stress is reached within the cohesive-zone, and that peak acceleration and peak velocity are reached only after some displacement. C, D. Observed evolutions of friction coefficient, slip-velocity and slip-acceleration and their relation to the displacement in two ELSE experiments (733 of SWG and 1059 in KD). Note that the x-axes are logarithmic. We noted general similarity to the idealized patterns in B.

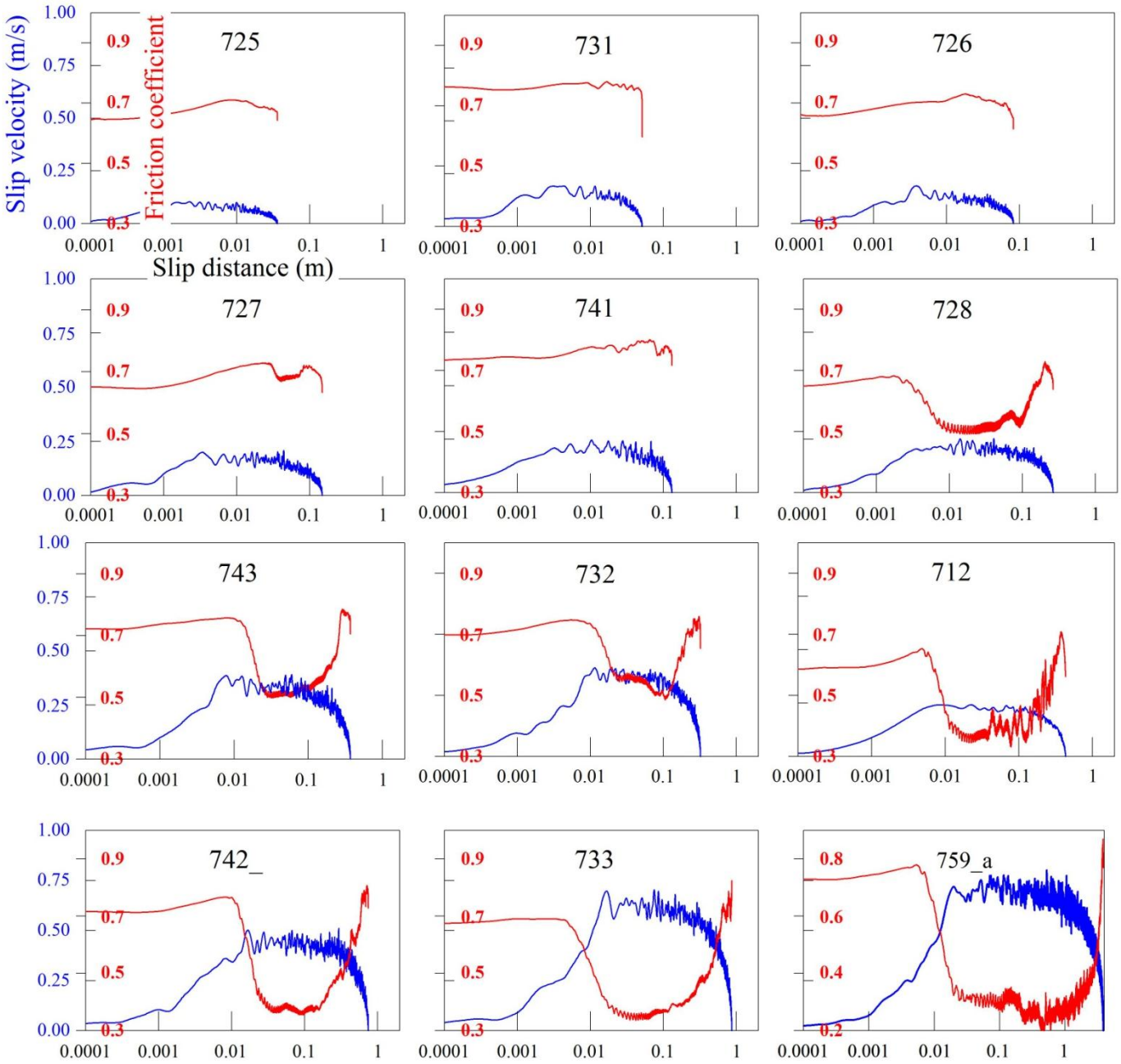

Fig. S7

Frictional strength (red) and slip velocity (blue) with respect to distance in selected Sierra White granite experiments (similar to Fig. 2 C). Same scales were used for all graphs excluding #759_a. The plots are arranged in an increasing order of peak-velocity (from left to right, top to bottom). Note that most runs show an initial strengthening for ~1 cm, and that the three runs in the upper rows, show negligible weakening.

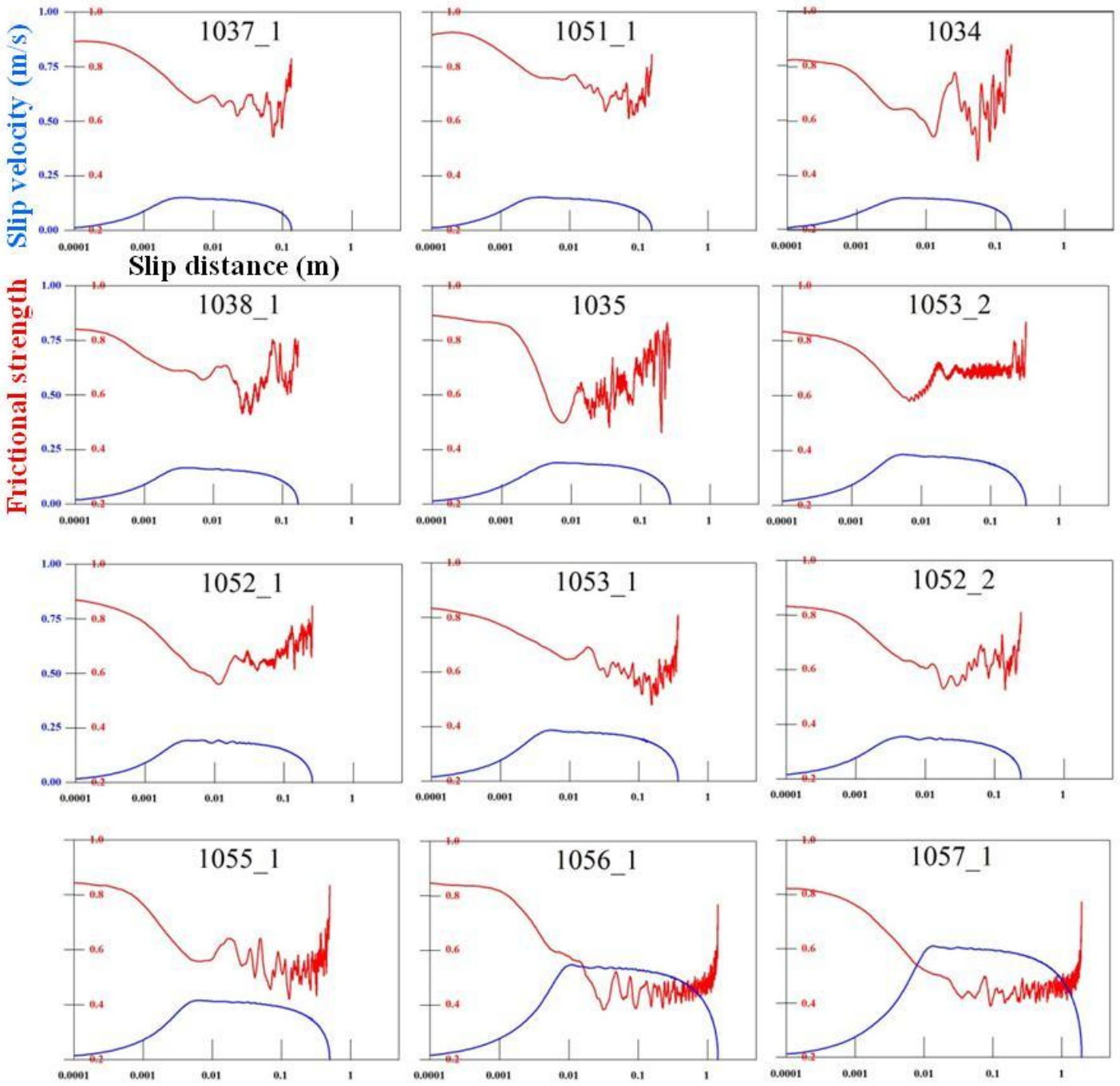

Fig. S8

Frictional strength (red) and slip velocity (blue) with respect to distance in selected Kasota dolomite experiments (similar to Fig. 2 D). Same scales were used for all graphs. The plots are arranged in an increasing order of peak-velocity (from left to right, top to bottom). Note that only two runs show a short strengthening stage, and all run showed dynamic weakening.

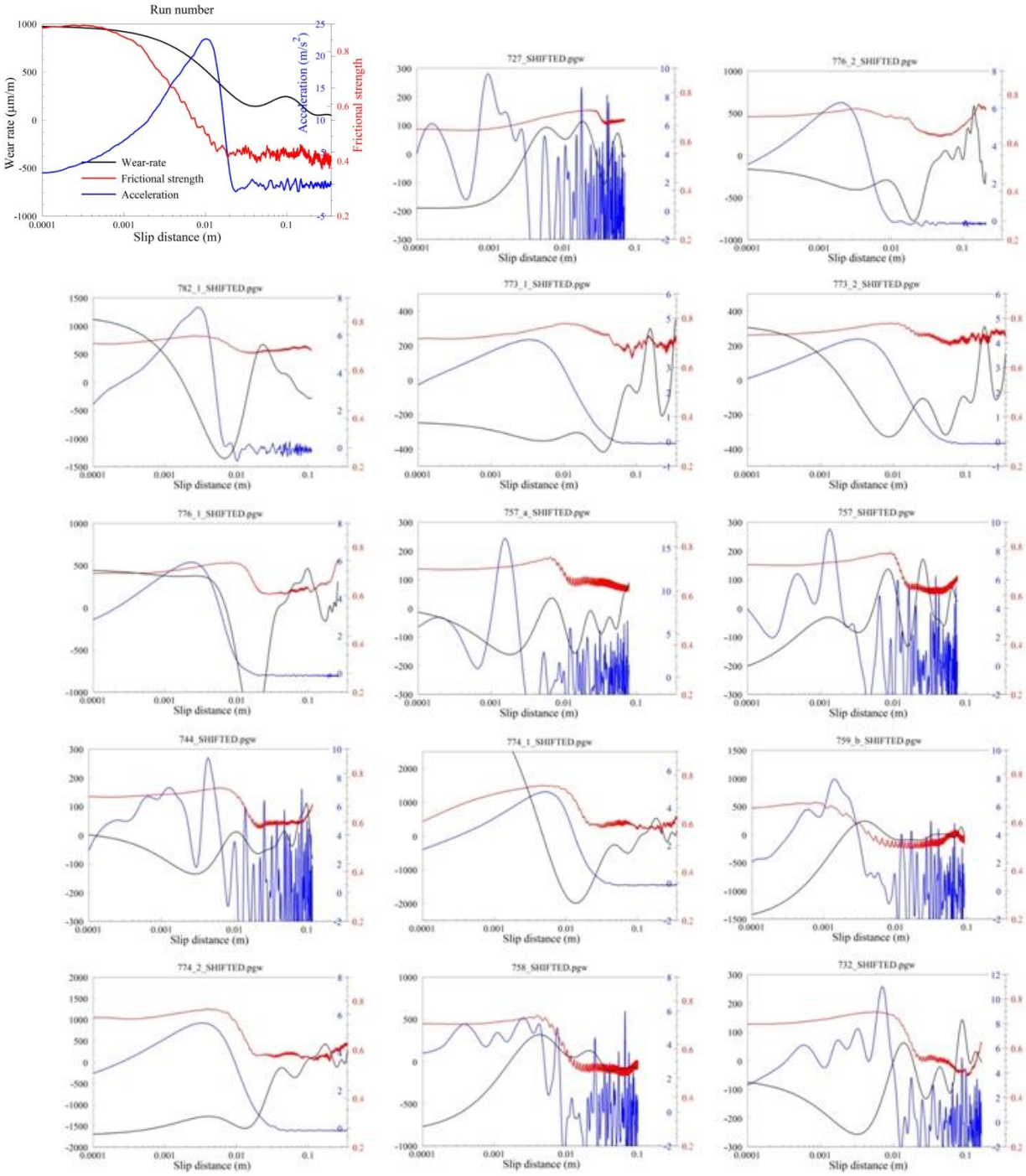
Run number
Wear rate (µm/m)
Acceleration (m/s²)
Frictional strength
Slip distance (m)
Wear-rate
Frictional strength
Acceleration
727_SHIFTED.pgw
776_2_SHIFTED.pgw
782_1_SHIFTED.pgw
773_1_SHIFTED.pgw
773_2_SHIFTED.pgw
776_1_SHIFTED.pgw
757_a_SHIFTED.pgw
757_SHIFTED.pgw
744_SHIFTED.pgw
774_1_SHIFTED.pgw
759_b_SHIFTED.pgw
774_2_SHIFTED.pgw
758_SHIFTED.pgw
732_SHIFTED.pgw

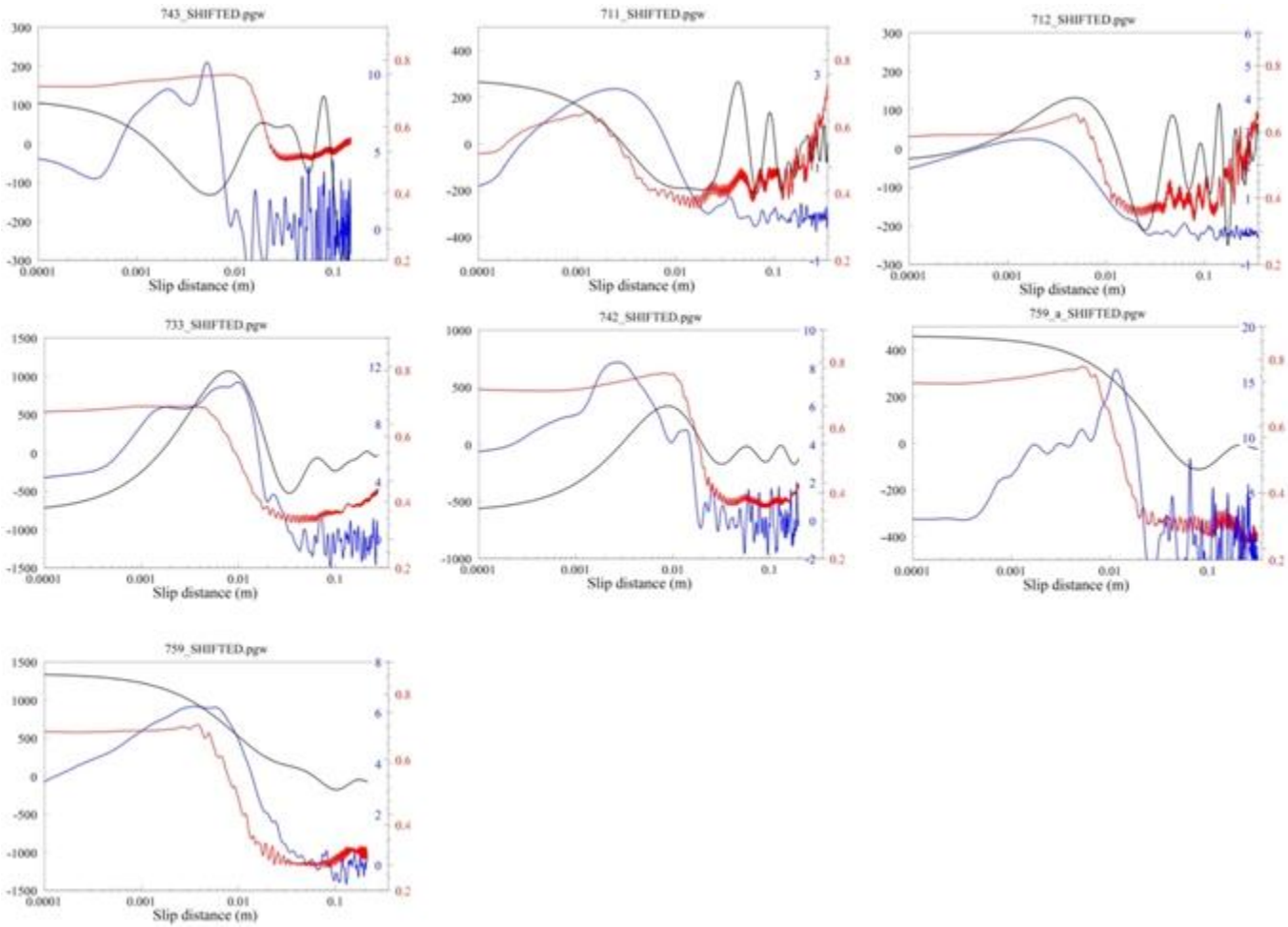

Fig. S9

Slip-acceleration (blue), strength-evolution (red) and fault wear-rate (black) during the first 0.35 m of slip in 22 Sierra White granite samples (Fig. 4A). Legend: upper left. Note: distance scale and frictional strength are the same for all plots, the acceleration, and wear-rate scales differ between the plots. See Figures 4 for d_C position. Similar acceleration-friction relations were presented in Fig. S5.

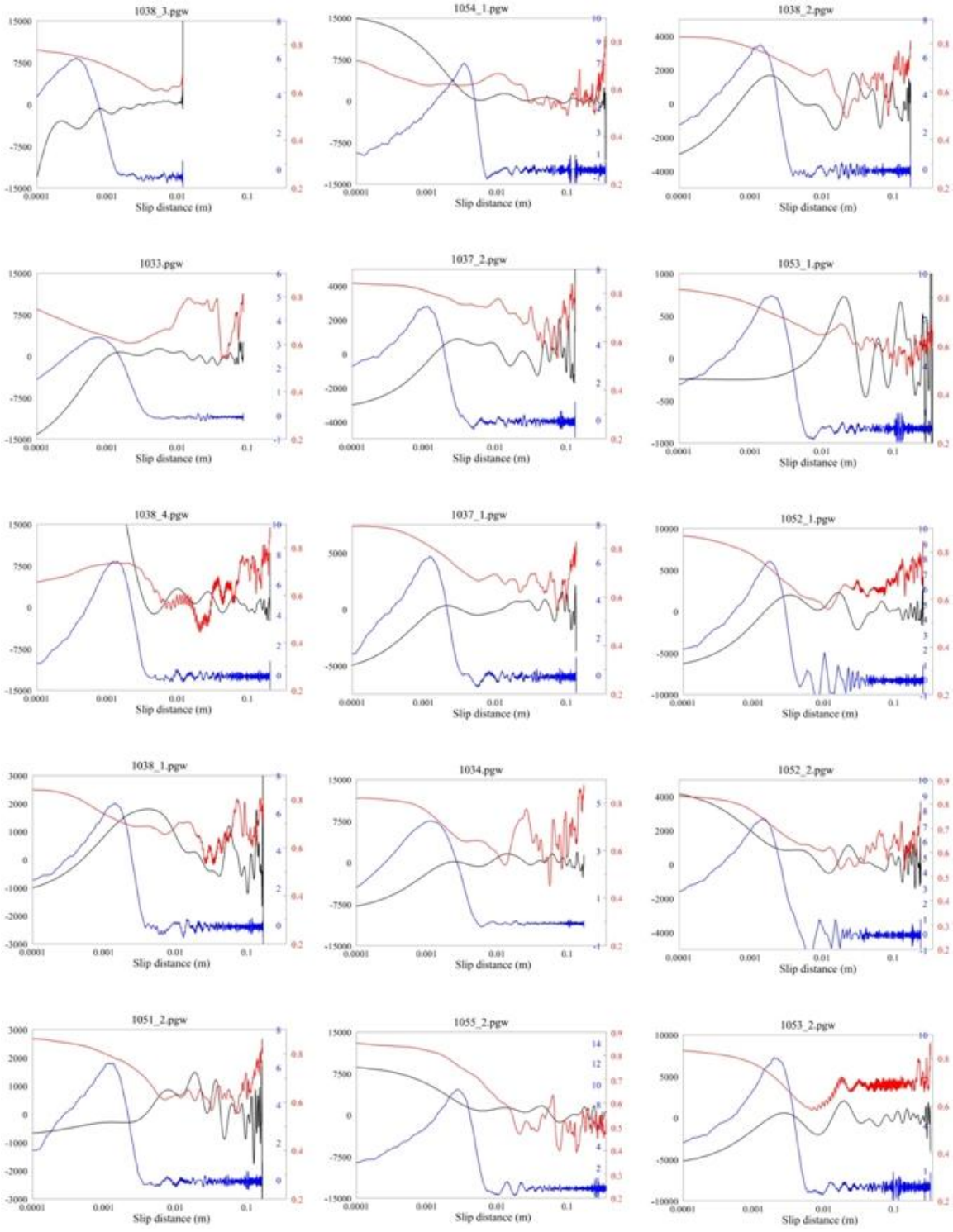
1038_3.pgw
1054_1.pgw
1038_2.pgw
1033.pgw
1037_2.pgw
1053_1.pgw
1038_4.pgw
1037_1.pgw
1052_1.pgw
1038_1.pgw
1034.pgw
1052_2.pgw
1051_2.pgw
1055_2.pgw
1053_2.pgw
Slip distance (m)

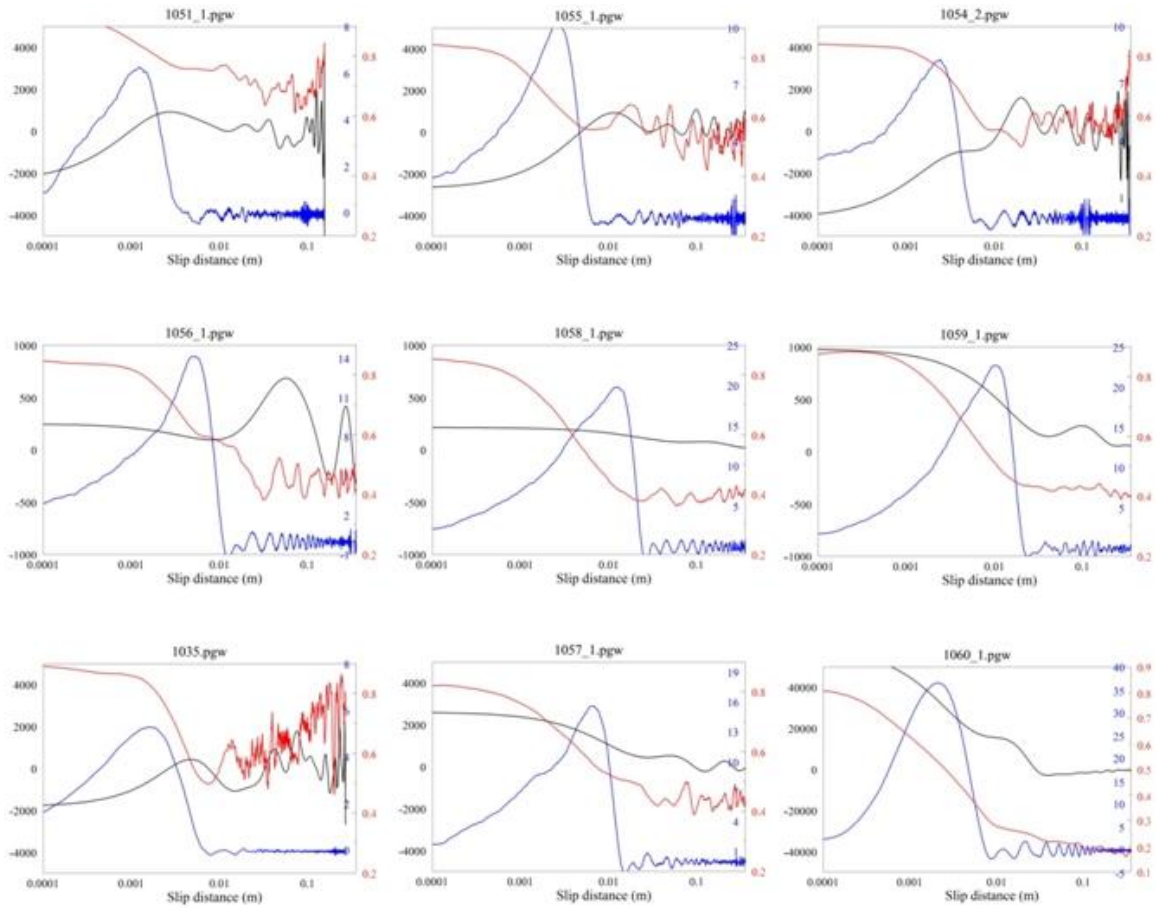

Fig. S10

Slip-acceleration (blue), strength-evolution (red) and fault wear-rate (black) during the first 0.35 m of slip in 24 Kasota dolomite (Fig. 4B). Legend in Fig. S9. Note: distance scale and frictional strength are the same for all plots, the acceleration, and wear-rate scales differ between the plots. See Figure 4 for d_C position.

Step	Fault patch during an earthquake	Flywheel-controlled ELSE experiment
I	Locked patch on a fault-zone in the crust.	A two-block sample (=experimental fault) is loaded to a selected normal stress; clutch #1 is engaged, clutch #2 is disengaged.
II	Interseismic period: increase of crustal elastic strain energy (=potential energy) around the fault. The shear/normal stress ratio reaches μ_o.	The flywheel is rotated to a prescribed velocity (=storing kinetic energy); clutch #1 is engaged, clutch #2 is disengaged.
III	Earthquake nucleation on the fault-zone away from the patch (Fig. 1A).	No sample-slip.
IV	Earthquake rupture front arrives at the patch (Fig. 1A); shear/normal stress increases.	Clutch #1 is disengaged & clutch #2 is engaged $\Rightarrow$ flywheel energy is transferred to sample $\Rightarrow$ shear stress on sample rises.
V	The shear/normal ratio increases to μ. If $\mu < \mu_S$ (static strength) $\Rightarrow$ patch remains locked, and if $\mu > \mu_S \Rightarrow$ patch slips (Fig. 1C).	If shear/normal stress ratio $< \mu_S$ (static strength) $\Rightarrow$ patch remains locked; If shear/normal stress ratio $> \mu_S \Rightarrow$ patch slips
VI	Patch may undergo dynamic weakening or hardening, generating, or not, an instability	Experimental patch may dynamically weaken or strengthen, generating, or not, an instability
VII	Patch slips distance D; slip terminates with no available energy or stresses below strength.	Sample slips for distance D; slip terminates with no available energy or stresses below strength.

Table S1.

The steps of the earthquake rupture process on a fault-patch, and the corresponding experimental procedure.

[a]Earthquake	[a]W_b MJ/m^2	[a]Average slip m	[b]Mean depth km	[b]Estimated normal stress		[b]Normalized fracture energy (m)	
				σ_{nU} (MPa)	σ_{nL} (MPa)	W_b/σ_{nU}	W_b/σ_{nL}
Imperial (1979)	1.82	0.60	5.25	89	27	2.0E-02	6.8E-02
	1.06	0.50	6.5	111	33	9.6E-03	3.2E-02
Landers (1992)	21.53	2.46	7.5	128	38	1.7E-01	5.6E-01
	14.91	1.88	7.5	128	38	1.2E-01	3.9E-01
Northridge (1994)	5.75	0.99	12	204	61	2.8E-02	9.4E-02
Morgan Hill (1984)	1.36	0.25	5	85	26	1.6E-02	5.3E-02
Western Tottori (2000)	1.69	0.99	9.25	157	47	1.1E-02	3.6E-02
	3.02	0.54	9.25	157	47	1.9E-02	6.4E-02
	2.73	0.55	9.25	157	47	1.7E-02	5.8E-02
Kobe (1995)	0.40	0.29	10	170	51	2.4E-03	7.8E-03
	0.97	0.42	10	170	51	5.7E-03	1.9E-02

[a] After (2).

[b] Calculations in present work.

Table S2.

Seismic and energy data for the six earthquakes analyzed by Tinti et al. (2005). Four of these earthquakes have more than one solution, and thus there are 11 separate solutions for their fracture energy. The presented values are the calculated averages for multiple sub-faults. The left three columns, marked by [a], are the original data(2), and the right five columns, marked by [b], are calculated here as explained above. The values of the fracture energy ratios (two right columns) are plotted versus the average slip (third column) in Fig. 3A.

Operator controlled parameters					Spontaneous fault patch response								Comments (neg. wk.= negligible weakening; no wk. =no weakening)
ELSE run #	Sampling rate (kHz)	Normalized energy density (m)	Maximum slip velocity (m/s)	Normal stress (MPa)	Maximum acceleration	Total Slip Distance (m)	Total time (rise time) (s)	Average frictional	Minimum frictional	Static frictional strength	Critical distance (m)	Maximum (initial) wear-rate (micron/m)	
711	**1**	**2.1E-01**	**0.25**	**2.0**	**5.2**	**0.42**	**3.4**	**0.57**	**0.36**	**0.43**	**0.015**	**1.3E+02**	
712	**1**	**2.2E-01**	**0.24**	**2.0**	**6.1**	**0.43**	**3.4**	**0.56**	**0.33**	**0.31**	**0.015**	6.3E+01	
721	5	1.5E-06	0.02	2.3	3.6							4.5E+04	no slip
722	5	5.8E-05	0.02	2.3	3.6							3.9E+04	no slip
723	5	4.0E-04	0.02	2.3	3.6								no slip
724	5	6.3E-03	0.06	2.3	5.8	0.01	0.5	0.63	0.61	0.62		1.1E+03	no wk.
725	**5**	**2.1E-02**	**0.10**	**2.3**	**8.3**	**0.04**	**0.9**	**0.68**	**0.61**	**0.61**		**1.1E+02**	neg. wk.
726	**5**	**5.2E-02**	**0.18**	**2.3**	**13.7**	**0.08**	**1.3**	**0.69**	**0.59**	**0.57**		**2.6E+02**	neg. wk.
727	**5**	**9.2E-02**	**0.21**	**2.3**	**13.7**	**0.15**	**1.8**	**0.69**	**0.63**	**0.65**	**0.037**	**3.2E+02**	
728	**5**	**1.4E-01**	**0.25**	**2.3**	**16.0**	**0.26**	**2.4**	**0.64**	**0.49**	**0.66**	**0.010**	**2.7E+02**	
731	**5**	**3.6E-02**	**0.19**	**6.9**	**17.1**	**0.05**	**0.6**	**0.76**	**0.60**	**0.78**	**0.012**	**7.7E+02**	
732	**5**	**1.8E-01**	**0.42**	**6.9**	**19.1**	**0.32**	**1.5**	**0.67**	**0.49**	**0.71**	**0.022**	**5.4E+02**	
733	**5**	**4.2E-01**	**0.70**	**6.8**	**28.8**	**0.87**	**2.5**	**0.62**	**0.34**	**0.66**	**0.047**	**1.6E+02**	
741	**5**	**8.6E-02**	**0.25**	**3.7**	**17.1**	**0.13**	**1.2**	**0.77**	**0.71**	**0.70**		**1.1E+02**	neg. wk.
742	**5**	**3.6E-01**	**0.51**	**3.7**	**26.1**	**0.74**	**3.0**	**0.64**	**0.35**	**0.73**	**0.034**	**1.0E+02**	
743	**5**	**2.0E-01**	**0.39**	**3.7**	**21.7**	**0.37**	**2.1**	**0.68**	**0.50**	**0.72**	**0.026**	**1.7E+02**	
744	**5**	**1.4E-01**	**0.33**	**3.7**	**17.0**	**0.24**	**1.6**	**0.71**	**0.58**	**0.72**	**0.021**	**1.7E+02**	
752	5	8.5E-05	0.16	1.9	36.3	0.00		0.40	0.27	0.26		1.5E+03	no slip
753	5	5.4E-04	0.02	1.9	3.6							1.2E+03	no slip
754	**5**	**7.1E-03**	**0.06**	**1.9**	**5.1**	**0.01**	**0.6**	**0.63**	**0.54**	**0.62**		**6.1E+02**	no wk.
755	5	2.6E-02	0.12	1.9	9.9	0.04	0.9	0.74	0.68	0.70		1.2E+02	no wk.
756	5	6.2E-02	0.16	1.9	9.4	0.09	1.4	0.77	0.70	0.74	0.092	1.9E+02	
757	**5**	**1.1E-01**	**0.20**	**1.9**	**14.2**	**0.18**	**2.0**	**0.72**	**0.61**	**0.73**	**0.014**	**6.4E+02**	
758	**5**	**1.8E-01**	**0.30**	**1.9**	**19.5**	**0.33**	**2.7**	**0.65**	**0.49**	**0.71**	**0.015**	**2.2E+02**	
759	**5**	**7.2E-01**	**0.55**	**1.9**	**27.0**	**1.73**	**6.5**	**0.50**	**0.27**	**0.69**	**0.017**	**2.8E+02**	
771	1	3.0E-02	0.07	1.8	2.1	0.03	1.0	0.70	0.09	0.08		3.6E+03	no wk.
772	1	1.9E-01	0.19	1.8	4.8	0.22	2.5	0.75	0.06	0.06		4.4E+02	neg. wk.
757_a	**5**	**1.1E-01**	**0.23**	**1.9**	**23.2**	**0.18**	**2.0**	**0.71**	**0.62**	**0.71**	**0.012**	**2.5E+02**	
759_a	**5**	**1.6E+00**	**0.80**	**2.0**	**33.1**	**3.86**	**9.5**	**0.49**	**0.19**	**0.74**	**0.023**	**9.9E+02**	
759_b	**5**	**5.8E-01**	**0.25**	**2.3**	**16.0**	**0.26**	**2.4**	**0.64**	**0.49**	**0.64**	**0.008**	**6.0E+02**	
773_1	**2**	**7.6E-01**	**0.39**	**1.8**	**10.3**	**0.94**	**4.9**	**0.75**	**0.59**	**0.58**	**0.065**	**1.4E+03**	
773_2	**2**	**7.6E-01**	**0.39**	**1.8**	**10.2**	**0.94**	**4.9**	**0.74**	**0.64**	**0.65**	**0.052**	**6.1E+02**	
774_1	**2**	**3.9E-01**	**0.38**	**3.6**	**8.8**	**0.59**	**3.0**	**0.69**	**0.49**	**0.49**	**0.019**	**7.5E+03**	
774_2	**2**	**3.8E-01**	**0.38**	**3.5**	**10.3**	**0.58**	**3.0**	**0.69**	**0.55**	**0.71**	**0.017**	**2.2E+03**	
775_1	2	1.7E-01	0.25	3.5	8.6	0.22	1.8	0.76	0.72	0.72		6.5E+02	neg. wk.
775_2	2	1.7E-01	0.25	3.5	8.5	0.24	1.9	0.71	0.63	0.71	0.028	1.2E+03	
776_1	**2**	**2.3E-01**	**0.29**	**3.3**	**8.9**	**0.33**	**2.3**	**0.70**	**0.61**	**0.63**	**0.022**	**1.4E+03**	

776_2	**2**	**1.7E-01**	**0.25**	**3.5**	**8.5**	**0.24**	**1.9**	**0.71**	**0.63**	**0.76**	**0.025**	**1.3E+03**	
776_3	2	3.3E-01	0.26	1.9	6.6	0.44	3.4	0.71	0.26	0.46		4.4E+04	neg. wk.
781_1	2	2.6E-01	0.25	2.1	7.0	0.17	1.4	0.61	0.38	0.37		4.5E+03	neg. wk.
781_2	2	2.7E-01	0.25	2.1	7.7	0.16	1.3	0.71	0.53	0.58		2.0E+03	neg. wk.
782_1	**5**	**2.9E-01**	**0.27**	**2.1**	**10.5**	**0.39**	**3.2**	**0.68**	**0.59**	**0.73**	**0.012**	**2.2E+03**	

Table S3

Table S3. Experimental data summary for 42 ELSE runs with Sierra White granite. Note the division into two blocks of parameters: four columns of experimental setting by the operator, and eight columns of experimental patch response. Data of experiments marked in **bold** are plotted either in the paper or here.

Operator controlled parameters					Spontaneous fault patch response								Comments
ELSE run #	Sampling rate	Normalized energy density (m)	Maximum slip velocity (m/s)	Average normal stress (MPa)	Maximum acceleration (ms2)	Total Slip Distance (m)	Total time (rise time) (s)	Average frictional strength	Minimum frictional strength	Static frictional strength	Critical distance (m)	Maximum wear-rate (micron/m)	
1033	**1**	**6.1E-02**	**0.11**	**1.8**	**3.0**	**0.09**	**1.5**	**0.71**	**0.53**	**0.85**	**0.002**	**1.8E+04**	
1034	**1**	**1.3E-01**	**0.15**	**1.6**	**4.0**	**0.17**	**2.2**	**0.73**	**0.45**	**0.60**	**0.012**	**3.1E+03**	
1035	**1**	**2.1E-01**	**0.19**	**1.6**	**4.9**	**0.27**	**2.8**	**0.73**	**0.46**	**0.68**	**0.003**	**2.4E+03**	
1037_1	**2**	**9.8E-02**	**0.15**	**2.1**	**5.9**	**0.13**	**1.8**	**0.70**	**0.54**	**0.77**	**0.004**	**3.1E+03**	
1037_2	**2**	**9.3E-02**	**0.15**	**2.2**	**5.7**	**0.13**	**1.7**	**0.72**	**0.53**	**0.85**	**0.038**	**1.4E+03**	
1038_1	**2**	**1.2E-01**	**0.17**	**2.1**	**6.2**	**0.17**	**2.0**	**0.70**	**0.53**	**0.85**	**0.006**	**5.8E+03**	
1038_2	**2**	**1.2E-01**	**0.17**	**2.1**	**6.3**	**0.17**	**2.1**	**0.69**	**0.49**	**0.82**	**0.021**	**3.6E+03**	
1038_3	**2**	**8.4E-03**	**0.09**	**2.9**	**5.4**	**0.01**	**0.3**	**0.65**	**0.60**	**0.67**	**0.004**	**1.2E+05**	
1038_4	**2**	**1.5E-01**	**0.17**	**1.7**	**7.1**	**0.21**	**2.4**	**0.73**	**0.44**	**0.59**	**0.005**	**7.1E+04**	
1051_1	**2**	**1.2E-01**	**0.15**	**1.8**	**5.9**	**0.15**	**2.1**	**0.73**	**0.61**	**0.76**	**0.003**	**1.6E+03**	
1051_2	**2**	**1.2E-01**	**0.15**	**1.8**	**5.9**	**0.16**	**2.1**	**0.71**	**0.55**	**0.79**	**0.005**	**2.6E+03**	
1052_1	**2**	**1.9E-01**	**0.19**	**1.8**	**7.4**	**0.26**	**2.7**	**0.72**	**0.56**	**0.80**	**0.009**	**2.9E+03**	
1052_2	**2**	**1.7E-01**	**0.19**	**2.0**	**7.1**	**0.24**	**2.5**	**0.66**	**0.53**	**0.82**	**0.014**	**2.9E+03**	
1053_1	**2**	**2.4E-01**	**0.23**	**2.0**	**8.3**	**0.37**	**3.1**	**0.64**	**0.48**	**0.82**	**0.030**	**1.6E+03**	
1053_2	**2**	**2.4E-01**	**0.23**	**2.0**	**8.1**	**0.32**	**2.8**	**0.73**	**0.58**	**0.78**	**0.005**	**2.9E+03**	
1054_1	**2**	**2.2E-01**	**0.23**	**2.2**	**6.6**	**0.34**	**2.9**	**0.63**	**0.49**	**0.80**	**0.027**	**6.8E+03**	
1054_2	**2**	**2.2E-01**	**0.23**	**2.2**	**7.8**	**0.34**	**2.9**	**0.64**	**0.50**	**0.83**	**0.006**	**9.0E+03**	
1055_1	**2**	**3.1E-01**	**0.27**	**2.2**	**9.7**	**0.50**	**3.6**	**0.60**	**0.42**	**0.77**	**0.002**	**9.1E+03**	
1055_2	**2**	**3.0E-01**	**0.27**	**2.2**	**9.0**	**0.50**	**3.6**	**0.59**	**0.39**	**0.85**	**0.018**	**7.4E+03**	
1056_1	**2**	**7.9E-01**	**0.43**	**2.1**	**13.6**	**1.40**	**6.3**	**0.52**	**0.38**	**0.83**	**0.022**	**8.5E+02**	
1057_1	**2**	**1.1E+00**	**0.51**	**2.2**	**15.0**	**1.95**	**7.4**	**0.52**	**0.39**	**0.72**	**0.024**	**1.9E+03**	
1058_1	**2**	**2.6E+00**	**0.79**	**2.2**	**19.4**	**4.63**	**11.2**	**0.49**	**0.34**	**0.79**	**0.014**	**6.6E+02**	
1059_1	**2**	**1.2E+00**	**0.77**	**4.6**	**22.0**	**2.55**	**6.5**	**0.46**	**0.35**	**0.75**	**0.013**	**2.2E+03**	
1060_1	**2**	**1.0E-01**	**0.53**	**28.8**	**32.7**	**0.47**	**1.7**	**0.22**	**0.16**	**0.80**	**0.005**	**4.0E+04**	

Table S4

Experimental data summary for 24 ELSE runs with Kasota dolomite. Note the division into two blocks of parameters: four columns of experimental setting by the operator, and eight columns of experimental patch response. Data of experiments marked in **bold** are plotted either in the paper or here.

References and notes

22. C. H. Scholz, *The Mechanics of Earthquakes and Faulting*, Cambridge U Press, London, 471 pp (2002).
23. H. Kanamori, E. E. Brodsky, The physics of earthquakes. *Rep. Prog. Phys*. **67**, 1429–1496, doi:10.1088/0034-4885/67/8/R03 (2004).
24. J. S. Chester, F. M. Chester, A. K. Kronenberg, Fracture surface energy of the Punchbowl fault, San Andreas system, *Nature* **437**, 133-136, doi:10.1038/nature03942 (2005).
25. Z. Reches Z, *Analysis of gouge powder from rupture-zone of recent earthquakes and rupture-zones developed in laboratory experiments*, Southern California Earthquake Center, Report 07085, retrieve by search at scec.org/core/cis/reportsearch.php (2007).
26. T. Rockwell, S. M. Girty, O. Dor, N. Wechsler, Y. Ben-Zion, Chemical and Physical Characteristics of Pulverized Tejon Lookout Granite Adjacent to the San Andreas and Garlock Faults: Implications for Earthquake Physics. *Pure Appl. Geophys*. 166, 1725–1746. Doi: 10.1007/s00024-009-0514-1 (2009).
27. T. Togo, T., Energy partition for grain crushing in quartz gouge during subseismic to seismic fault motion: An experimental study. *J. Structural Geol.* 38, 139-155 (2012).
28. M. Sawai, T. Shimamoto, T. Togo, Reduction in BET surface area of Nojima fault gouge with seismic slip and its implication for the fracture energy of earthquakes. . *J. Structural Geol.* 38, 117-138 (2012).
29. A. Piatanesi, E. Tinti, M. Cocco, E. Fukuyama, The dependence of traction evolution on the earthquake source time function adopted in kinematic rupture models. *Geoph. Res. Lett.*, **31**, doi: 10.1029/2003GL019225 (2005).
30. G. DiToro *et al.*, Fault lubrication during earthquakes. *Nature* **471**, 494-498 (2011).
31. F. Yuan, V. Prakash, Slip weakening in rocks and analog materials at co-seismic slip rates. *J Mech. Phys. Solids* 56, 542-560 (2008).
32. A. Tsutsumi, and T. Shimamoto, High-velocity frictional properties of gabbro, *Geophys. Res. Lett.*, 24, 699–702, (1997)doi:10.1029/97GL00503.
33. T. Hirose, and T. Shimamoto, Growth of molten zone as a mechanism of slip weakening of simulated faults in gabbro during frictional melting, *J. Geophys. Res.*, 110, B05202, (2005)doi:10.1029/2004JB003207.
34. N. Tisato, G. Di Toro, N. De Rossi, M. Quaresimin, & T. Candela. Experimental investigation of flash weakening in limestone. *J. Structure Geol*. **38,** 183-199 (2012).
35. M. S. Boettcher, A. McGarr, M. Johnston, Extension of Gutenberg-Richter distribution to MW -1.3, no lower limit in sight. *Geophys. Res. Lett*. **36,** L10307 (2009), doi:10.1029/2009GL038080.
36. Y. Yabe *et al.*, Observation of numerous aftershocks of an M_W 1.9 earthquake with an AE network installed in a deep gold mine in South Africa. *Earth Planets Space* **61**, e49–e52 (2009).